

The SPHINX cosmological simulations of the first billion years: the impact of binary stars on reionization

Joakim Rosdahl,¹★ Harley Katz,^{2,3} Jérémy Blaizot,¹ Taysun Kimm,^{3,4}
Léo Michel-Dansac,¹ Thibault Garel,¹ Martin Haehnelt,³ Pierre Ocvirk⁵ and
Romain Teyssier⁶

¹Univ Lyon, Univ Lyon1, Ens de Lyon, CNRS, Centre de Recherche Astrophysique de Lyon UMR5574, F-69230 Saint-Genis-Laval, France

²Subdepartment of Astrophysics, University of Oxford, Keble Road, Oxford OX1 3RH, UK

³Kavli Institute for Cosmology and Institute of Astronomy, Madingley Road, Cambridge CB3 0HA, UK

⁴Department of Astronomy, Yonsei University, 50 Yonsei-ro, Seodaemun-gu, Seoul 03722, Republic of Korea

⁵Observatoire Astronomique de Strasbourg, Université de Strasbourg, CNRS UMR 7550, 11 rue de l'Université, F-67000 Strasbourg, France

⁶Institute for Computational Science, University of Zürich, Winterthurerstrasse 190, CH-8057 Zürich, Switzerland

Accepted 2018 June 17. Received 2018 June 04; in original form 2018 January 19

ABSTRACT

We present the SPHINX suite of cosmological adaptive mesh refinement simulations, the first radiation-hydrodynamical simulations to simultaneously capture large-scale reionization and the escape of ionizing radiation from thousands of resolved galaxies. Our 5 and 10 co-moving Mpc volumes resolve haloes down to the atomic cooling limit and model the interstellar medium with better than ≈ 10 pc resolution. The project has numerous goals in improving our understanding of reionization and making predictions for future observations. In this first paper, we study how the inclusion of binary stars in computing stellar luminosities impacts reionization, compared to a model that includes only single stars. Owing to the suppression of galaxy growth via strong feedback, our galaxies are in good agreement with observational estimates of the galaxy luminosity function. We find that binaries have a significant impact on the timing of reionization: with binaries, our boxes are 99.9 percent ionized by volume at $z \approx 7$, while without them our volumes fail to reionize by $z = 6$. These results are robust to changes in volume size, resolution, and feedback efficiency. The escape of ionizing radiation from individual galaxies varies strongly and frequently. On average, binaries lead to escape fractions of ≈ 7 –10 percent, about three times higher than with single stars only. The higher escape fraction is a result of a shallower decline in ionizing luminosity with age, and is the primary reason for earlier reionization, although the higher integrated luminosity with binaries also plays a subdominant role.

Key words: methods: numerical – galaxies: high-redshift – dark ages, reionization, first stars – early Universe.

1 INTRODUCTION

The formation of the first galaxies marks the end of the dark ages and the beginning of the Epoch of Reionization (EoR). Radiation from the first generations of stars, hosted by the first galaxies, heated the surrounding intergalactic gas via photoionization. As the ionized hydrogen (H II) bubbles grew and percolated, the whole Universe was transformed from a dark, cold, neutral state into a hot ionized one: reionization was completed. This last major transition of the Universe is at the limit of our observational capabilities and is a

key science driver of the foremost upcoming telescopes, such as the *James Webb Space Telescope* (JWST) and the Square Kilometre Array (SKA).

Cosmological simulations are an indispensable tool to disentangle the complex and non-linear interplay of physical mechanisms leading to reionization, a ‘loop’ encompassing an enormous range of physical scales: of gravitational collapse of dark matter (DM) into haloes, the condensation of gas via radiative cooling into galaxies at the centres of those haloes, its eventual collapse into stars, which is slowed down by feedback, the emission of ionizing radiation from those stars, the propagation of the radiation through the interstellar medium (ISM), the circumgalactic medium (CGM) and the inter-

* E-mail: karl-joakim.rosdahl@univ-lyon1.fr

galactic medium (IGM), and its ability to suppress gas cooling and thus star formation (SF).

Two major challenges face those seeking to understand reionization with simulations, compared with simulations of galaxy evolution at low redshift. First is the need for radiation-hydrodynamics (RHD) to explicitly model the interplay of ionizing radiation and gas. Traditional cosmological simulations use pure gravitohydrodynamics, typically applying homogeneous ultraviolet (UV) background radiation instead of the more computationally expensive hydrodynamically coupled radiative transfer (RT). However, to model the reionization process self-consistently, the radiation should not be ignored or applied in post-processing. The second challenge is capturing the range of scales involved. Reionization is a large-scale process that should preferentially be modelled on cosmological-homogeneity scales, or volume widths of $\gtrsim 200$ co-moving Mpc (cMpc), in order to predict the patchiness of reionization and a realistic average volume filling factor of ionized gas that is unaffected by cosmic variance (Iliev et al. 2013). The sources of reionization, however, form and emit radiation on relatively tiny, subpc scales, and even if subpc scales are not represented, predicting the transfer and escape of ionizing radiation through the ISM requires at least a few pc resolution (e.g. Kimm & Cen 2014; Xu et al. 2016).

There has been a surge of cosmological RHD reionization simulation projects that have captured the large-scale reionization process (Gnedin & Fan 2006; Finlator, Dave & Ozel 2011; Iliev et al. 2013; Gnedin 2014; So et al. 2014; Ocvirk et al. 2015; Pawlik et al. 2016; Chen et al. 2017), with volume widths ranging from ~ 10 to 600 cMpc. However, the range of scales required to adequately model *both* the large-scale process and the production and transfer of radiation through the ISM has been out of reach. Galaxies are still largely unresolved in reionization simulations, with physical resolution ranging from ~ 100 pc (Gnedin 2014; Pawlik et al. 2016) for smaller volumes to 100 kpc (Iliev et al. 2013) for the largest ones. Therefore, the escape fraction of ionizing radiation from galaxies, f_{esc} , is fully or partly a free and adjustable parameter. If galaxies are not resolved at all, it sets the total fraction of radiation getting out of galaxies. If galaxies are to some degree resolved, the free parameter is a subresolution escape fraction, f'_{esc} , setting the luminosity of stellar sources, and the real escape fraction becomes a multiple of f'_{esc} , which sets the production rate of ionizing photons, and the fraction of emitted radiation that propagates out of galaxies (e.g. Pawlik et al. 2016).

Cosmological *zoom* simulations can achieve a much higher maximum resolution than full cosmological simulations by focusing only on the environment of one or a few haloes with a nested refinement structure. In this type of simulation, the production and escape of ionizing radiation in galaxies can be predicted in detail, even with subparsec resolution. Furthermore, fewer assumptions regarding SF, feedback, and radiation-gas interactions are required. Radiation-hydrodynamical zoom simulations have provided important insight into reionization and particularly how f_{esc} appears to highly fluctuate and be strongly regulated by feedback (Wise & Cen 2009; Kimm & Cen 2014; Wise et al. 2014; Xu et al. 2016; Kimm et al. 2017; Trebitsch et al. 2017a). However, the sacrifice is that the large-scale reionization process, statistical averages, and the scatter (in e.g. f_{esc} and ionizing luminosities against galaxy properties) provided by the resolved evolution of many haloes is lost. The cosmological environment surrounding these few targeted well-resolved haloes remains at a relatively low resolution and only serves to provide a realistic background gravitational field.

The recent state-of-the-art is to connect these two types of small-scale and large-scale simulations by using the predicted escape of

photons from the high-resolution zooms as inputs for the unresolved escape of photons from galaxies in full reionization simulations, allowing predictions to be made for the contributions of different galaxy masses to reionization (Xu et al. 2016; Chen et al. 2017). Yet, this approach still lacks the full coupling between the highly fluctuating escape of ionizing radiation from these unresolved galaxies and the galaxy dynamics, which is partially regulated by large-scale processes of mergers and accretion. Full non-zoom cosmological RHD simulations of reionization that capture these large-scale processes and simultaneously predict the production and escape of ionizing radiation remain the ideal goal.

With recent increase in computational power and algorithmic advances for RHD in the RAMSES-RT code, this goal is now within reach. Here, we present the SPHINX¹ suite of simulations, a series of cosmological volumes 5–10 cMpc in width where haloes are well resolved down to or below the atomic cooling threshold (halo mass of $M_{\text{vir}} \approx 3 \times 10^7 M_{\odot}$; Wise et al. 2014) and a maximum physical resolution of 11 pc is reached in the ISM of galaxies at $z = 6$ (and higher at higher redshifts).

These volumes are still well below the cosmological homogeneity scale, but we apply an initial conditions (ICs) selection technique that allows us to minimize cosmic variance effects, model an accurate ionizing photon production rate, and achieve reionization histories that are well converged with simulation volume. The simulation volumes include thousands of star-forming galaxies, allowing for a statistical understanding of escape fractions and ionizing luminosities for haloes over a mass range of $\sim 10^7$ – $10^{11} M_{\odot}$.

Our goals with the SPHINX project are numerous, including understanding the main sources of reionization (e.g. halo masses, environments, stellar population ages), the statistical behaviour of f_{esc} , and the back-reaction (Gnedin & Kaurov 2014) of radiation on the formation of dwarf galaxies. Furthermore, we aim to make predictions for the observational signatures of EoR galaxies for the *JWST* and to better constrain the metal enrichment process of the high-redshift IGM. These goals will be addressed in forthcoming papers. This pilot SPHINX paper is dedicated to describing the numerical methods and setup of our simulations, to comparing our simulated galaxies to observations of the high-redshift Universe, and to addressing the contribution of binary stars to reionization.

Recently, Stanway, Eldridge & Becker (2016) demonstrated how accounting for the interactions of binary stars in spectral energy distribution (SED) models increases the total flux of ionizing radiation from metal-poor stellar populations by tens of percent, compared to models that do not include binaries. Around the same time, Ma et al. (2016) demonstrated an additional, and perhaps more important, effect of binaries, which is an increase in the escape of ionizing radiation from galaxies. They post-processed cosmological zoom simulations with ray-tracing, comparing two sets of SED models, with only single stars, and with added binary stars, and found a factor 4–10 higher f_{esc} with binary stars included (with $f_{\text{esc}} \gtrsim 20$ per cent for binaries).

This ties to the regulation of f_{esc} by stellar feedback. In the first few million years after the birth of a stellar population, very little ionizing radiation escapes, even if the population is very luminous, since the radiation is absorbed locally by the dense ISM. The first SN explosions at ≈ 3 Myr coincide with a steep drop in the production rate of ionizing photons, because the most luminous stars in the population are precisely those most massive ones that explode first

¹In the spirit of the mythical SPHINX, we prefer to keep the acronym an enigma.

as SNe. So as the ISM starts to be cleared away by SN explosions and the radiation begins to escape, the ionizing luminosity is rapidly declining, resulting in an overall small fraction of the emitted radiation escaping. Due to mass transfer and mergers between binary companions, UV luminous stars exist at much later times in models that include binaries compared to single stars only models. The luminosity still declines after 3 Myr, but at a slower rate, enhancing the number of photons that can escape into the IGM *after* the onset of SN explosions.

Ma et al. (2016) predict a strong boost in f_{esc} with the inclusion of binary stars, but they apply the RT in post-processing and only consider three galaxies from cosmological zoom simulations. Therefore, they do not consider the back-reaction on the gas or predict how binary stars affect the reionization history. In this paper, we seek to verify and expand the results of Ma et al. (2016), using directly coupled RHD, and a full (non-zoom) cosmological volume to provide the statistics of thousands of galaxies. This allows us to directly probe whether and how the inclusion of binary stars affects the evolution, observational properties, and escape fractions of galaxies, as well as the timing and the process of reionization.

The setup of the paper is as follows. In Section 2, we present our simulation methods and setup (code, refinement, RT, SF, feedback, selection of ICs). In Section 3, we present our results, first comparing our simulations with $z = 6$ observables, then showing the reionization histories resulting from binary and single-star SED models, and finally comparing overall escape fractions, with those same models, from millions of stellar populations in thousands of galaxies. We present our discussion of the greater impact of binaries on reionization in Section 4 and conclude in Section 5 by highlighting upcoming work using the SPHINX simulations.

2 SIMULATIONS

We use RAMSES-RT (Rosdahl et al. 2013; Rosdahl & Teyssier 2015), which is an RHD extension of the cosmological gravitohydrodynamical code RAMSES (Teyssier 2002),² to solve the interactions of DM, stellar populations, ionizing radiation, and baryonic gas via gravity, hydrodynamics, RT, and non-equilibrium radiative cooling/heating, on a three-dimensional adaptive mesh. For the hydrodynamics, we use the HLLC Riemann solver (Toro, Spruce & Speares 1994) and the MinMod slope limiter to construct gas variables at cell interfaces from their cell-centred values. To close the relation between gas pressure and internal energy, we use an adiabatic index $\gamma = 5/3$, which is appropriate for an ideal monatomic gas. The dynamics of collisionless DM and stellar particles are evolved with a particle-mesh solver and cloud-in-cell interpolation (Guillet & Teyssier 2011). The advection of radiation between cells is solved with a first-order moment method, using the fully local M1 closure for the Eddington tensor (Levermore 1984) and the Global-Lax-Friedrich flux function for constructing the inter-cell radiation field.

In the following subsections, we describe the set-up of our simulations (ICs, adaptive refinement, ionizing radiation, thermochemistry), our main subgrid model components (SF and supernova feedback), and the halo finder utilized in the analysis. For reference, the main simulation parameters are listed in Table 1.

²The public code, including all the RHD extensions used here, can be downloaded at <https://bitbucket.org/rteyssie/ramses>.

Table 1. Simulation parameters, by name, value, and description.

Name	Value	Comments
Ω_m	0.3175	ICs mass density
Ω_Λ	0.6825	ICs dark energy density
Ω_b	0.049	ICs baryon density
σ_8	0.83	ICs amplitude of galaxy fluctuations
H_0	67.11 km s ⁻¹ Mpc ⁻¹	Hubble constant
X	0.74	Hydrogen mass fraction
Y	0.24	Helium mass fraction
Z_{init}	$3.2 \times 10^{-4} Z_\odot$	Initial metal mass fraction
η_{SN}	0.2	SN ejecta mass fraction
m_{SN}	$5 M_\odot$	Mean SN progenitor mass
y	0.075	SN metal yield

2.1 Halo finder

For identification of haloes and galaxies, we use the ADAPTAHOP halo finder (Aubert, Pichon & Colombi 2004; Tweed et al. 2009) in the most massive submaxima (MSM) mode. We fit a tri-axial ellipsoid to each (sub)halo and check that the virial theorem is satisfied within this ellipsoid, with the centre corresponding to the location of the densest particle. If this condition is not satisfied, we iteratively decrease its volume until we reach an inner virialized region. From the volume of this largest ellipsoidal virialized region, we define the virial radius R_{vir} and mass M_{vir} . We have checked that our results are similar if we instead use M_{200} and R_{200} , defined to produce a spherical overdensity 200 times the critical value. For the halo finder, we require a minimum of 20 particles per halo. In practice, using the notation of Aubert et al. (2004, App. B) we use for the halo finder $N_{\text{SPH}} = 32$, $N_{\text{HOP}} = 16$, $\rho_{\text{TH}} = 80$, and $f_{\text{Poisson}} = 4$. We also require that a (sub)group of particles has at least 20 particles during the halo/subhalo decomposition step. In the end, we retain for the analysis only those haloes we consider resolved, with $M_{\text{vir}} > 300 m_{\text{DM}}$, where m_{DM} is the DM particle mass. For this work, we also ignore subhaloes in our analysis.

We also identify galaxies with ADAPTAHOP. Here, we require at least 10 stellar particles per galaxy and we add subgroups to the main bodies. The galaxy-finder parameters are: $N_{\text{SPH}} = 10$, $N_{\text{HOP}} = 10$, $\rho_{\text{TH}} = 10^4$, and $f_{\text{Poisson}} = 4$.

2.2 Initial conditions

We generate the cosmological ICs with MUSIC (Hahn & Abel 2011). Our Λ cold dark matter universe has cosmological parameters $\Omega_\Lambda = 0.6825$, $\Omega_m = 0.3175$, $\Omega_b = 0.049$, $h \equiv H_0/(100 \text{ km s}^{-1} \text{ Mpc}^{-1}) = 0.6711$, and $\sigma_8 = 0.83$, consistent with the Planck 2013 results (Planck Collaboration I 2014). We assume hydrogen and helium mass fractions $X = 0.76$ and $Y = 0.24$, respectively, and the gas is given an initial homogeneous metal mass fraction of $Z_{\text{init}} = 6.4 \times 10^{-6} = 3.2 \times 10^{-4} Z_\odot$ (we assume a solar metal mass fraction of $Z_\odot = 0.02$ throughout this work). This unrealistically non-pristine initial metallicity is used to compensate for our lack of molecular hydrogen cooling channels in the infant Universe, allowing the gas to cool below 10^4 K, and calibrated so that the first stars form at redshift $z \approx 15$.

We use three sets of ICs with two volume sizes, as listed in Table 2. Our main simulation volume, s10_512, has a width of 10 cMpc, a minimum (coarse) physical resolution of 19.6 ckpc (2.8 kpc at $z = 6$), and reaches a maximum cell resolution of 76.3 cpc (10.9 pc at $z = 6$). It is populated by 512^3 DM particles with mass $m_{\text{DM}} = 2.6 \times 10^5 M_\odot$ each. We assume the limit of a resolved halo

Table 2. Simulation volumes used in this work. The table columns are as follows, from left to right: Name: simulation name, with the first number denoting the volume width and the second number denoting the number of resolution elements (DM particles, coarse cells) per dimension. L_{box} : volume width. Δx_{max} : physical width of coarsest grid cells. Δx_{min} : physical width of finest grid cells. m_{DM} : mass of DM particles. m_* : minimum initial mass of stellar particles (most particles have this initial mass, but some have an integer multiple of it).

Name	L_{box} (cMpc)	Δx_{max} ($z = 6$)	Δx_{min} ($z = 6$)	m_{DM} (M_{\odot})	m_* (M_{\odot})
s10_512	10	2.8 kpc	10.9 pc	2.5×10^5	10^3
s05_512	5	1.4 kpc	10.9 pc	3.1×10^4	10^3
s05_256	5	2.8 kpc	10.9 pc	2.5×10^5	10^3

being at a mass corresponding to 300 DM particles. This means we resolve haloes down to a mass of $M_{\text{vir}} \approx 7.5 \times 10^7 M_{\odot}$, which is slightly above the atomic cooling limit of $M_{\text{vir}} \approx 3 \times 10^7 M_{\odot}$ (Wise et al. 2014). The atomic cooling limit is important because below it, primordial galaxies form inefficiently and likely contribute little to reionization due to their self-destructive behaviour (Kimm et al. 2017). To measure the possible contribution from low-mass haloes that are above the atomic cooling limit but unresolved in the s10_512 volume (i.e. at masses $\approx 3 \times 10^7 - 10^8 M_{\odot}$), we use volume s05_512, with the same number of DM particles but half the width, thus giving an eight times higher DM mass resolution, or $m_{\text{DM}} = 3.1 \times 10^4 M_{\odot}$, and haloes resolved down to $M_{\text{vir}} \approx 10^7 M_{\odot}$. Statistical representation of massive haloes is sacrificed, due to the smaller volume, to the gain of resolving haloes down to the atomic cooling limit. This allows us to probe the contribution of the smallest haloes to reionization. We keep the maximum physical resolution in this volume the same as in s10_512, i.e. 10.9 pc at $z = 6$, but the coarse resolution is higher, following the DM resolution, or 1.4 kpc at $z = 6$.

The third simulation volume, s05_256, connects the other two volumes by having the resolution of the larger volume, s10_512, and size and ICs of the smaller volume, s05_512. Hence we can use it for resolution convergence studies, by comparing the properties of galaxies to those in s05_512.

2.2.1 Volume selection

Our simulation volumes do not probe the scales at which the Universe is homogeneous. Hence we are influenced by cosmic variance, such that different IC realizations, with different random seeds for the generation of density fluctuations, result in different halo mass functions at later epochs. This can, in turn, affect the luminosity function and change the reionization history.

To recover a representative luminosity density and reionization history from our limited-volume simulations, we seek to minimize the effects of cosmic variance on the ionizing luminosity budget by selecting the most representative ICs from a large set of candidates. We perform 60 pure DM simulations at a degraded resolution of 256^3 for both the 10 and 5 cMpc wide volumes, each starting from ICs generated with a unique set of random number seeds. We then select from those the ICs that give the most average cumulative DM halo mass function to the power of 1.5, $M_{200}^{1.5}$, at $z = 10, 8,$ and 6 . We use $M_{200}^{1.5}$ rather than M_{200} because we find that it correlates better with the total luminosity of galaxies: the ionizing luminosity scales linearly with the star formation rate (SFR), which scales roughly as $M_{200}^{1.5}$ (see Fig. 6).

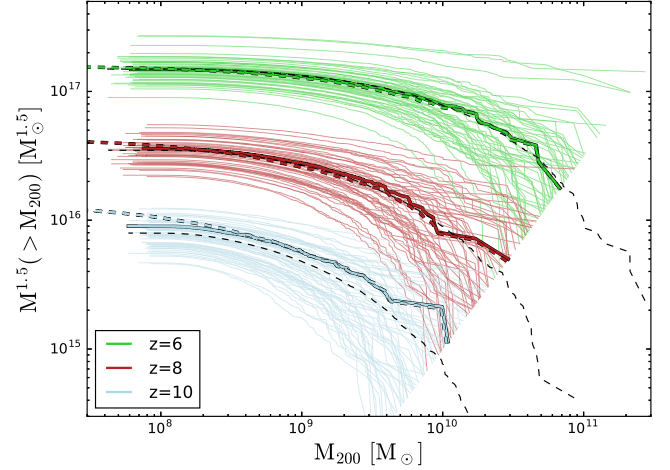


Figure 1. Cumulative power – 1.5 halo mass functions at $z = 10, 8,$ and 6 , as indicated in the legend, in 256^3 – resolution pure DM simulations run from 60 IC realizations for 10 cMpc volumes (thin coloured curves). The dashed black curves show the averages of all the simulations at the same redshifts, and the solid thick coloured curves represent the IC seeds we have selected for the production (10 cMpc) SPHINX simulations to best match the averages at all three redshifts. The dashed coloured curves represent the same seeds for a non-degraded DM mass resolution of 512^3 .

Fig. 1 shows the cumulative $M_{200}^{1.5}$ functions at $z = 10, 8,$ and 6 for the 60 pure DM runs of the 10 cMpc ICs in coloured curves, and the averages of all 60 simulations in thick dashed black curves. Our selected ICs are represented by thick coloured curves, at the degraded 256^3 DM mass resolution in solid and the fiducial 512^3 resolution in dashed. A comparison of the thick coloured solid and dashed curves shows that the DM resolution has little effect on the cumulative halo mass function (but note that it does have an impact on the non-cumulative function at the low-mass end, since low-mass haloes are lost when degrading the resolution). Out of 60 candidate ICs, it is difficult to get an ideal average at all three redshifts. The selected ICs are very close to the average at $z = 6$ and 8 , but slightly top-heavy at $z = 10$ and thus perhaps produce slightly too many stars at $z \gtrsim 10$.

Fig. 2 shows the number of haloes in our two simulation volumes, binned by halo mass. At $z = 6$, each volume contains about 5800 haloes above the resolution limit. The smaller and larger volumes have maximum halo masses of $M_{\text{vir}} = 1.1 \times 10^{10} M_{\odot}$ and $4.7 \times 10^{10} M_{\odot}$, respectively, at $z = 6$.

2.3 Adaptive refinement

In the cubical octree structure of RAMSES, the cell refinement level ℓ sets the cell width $\Delta x_{\ell} = 0.5^{\ell} L_{\text{box}}$, where L_{box} is the width of the volume. Taking our 10 cMpc volume, the coarsest level is $\ell_{\text{min}} = 9$, corresponding to $2^{\ell} = 512$ coarse cell widths and a minimum resolution of 19.6 ckpc (2.8 kpc at $z = 6$). Starting at this coarsest level, cells are adaptively refined to higher levels, up to $\ell_{\text{max}} = 17$, which corresponds to a maximum physical resolution of 10.9 pc at $z = 6$.

A cell is flagged for refinement into eight equally sized children cells if: (i) $M_{\text{DM, cell}} + \frac{\Omega_{\text{m}}}{\Omega_{\text{b}}} M_{\text{baryons, cell}} > 8 m_{\text{DM}}$, where $M_{\text{DM, cell}}$ and $M_{\text{baryons, cell}}$ are the total DM and baryonic (gas plus stars) masses in the cell, or (ii) the cell width is larger than a quarter of the local

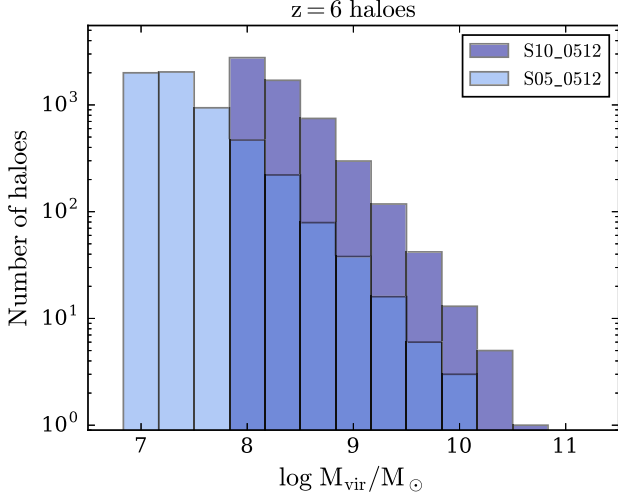


Figure 2. Number of $z = 6$ haloes, binned by virial mass (M_{vir}), for our two main volumes; the high DM–mass resolution 5 cMpc volume (light blue) and the fiducial resolution 10 cMpc volume (darker blue). At this redshift, each volume contains approximately 5800 haloes above the resolution limit of 300 DM particles (corresponding to a DM mass of $10^7 M_{\odot}$ for the smaller volume and $8 \times 10^7 M_{\odot}$ for the larger volume).

Jeans length,

$$\lambda_J = \sqrt{\frac{\pi c_s^2}{G \rho}} = 16 \text{ pc} \left(\frac{T}{1 \text{ K}} \right)^{1/2} \left(\frac{n_H}{1 \text{ cm}^{-3}} \right)^{-1/2}, \quad (1)$$

where $c_s = \sqrt{\gamma k_B T / m_p}$ is the speed of sound, G the gravitational constant, ρ the gas mass density, and n_H the hydrogen number density.

Contrary to the default refinement strategy in *RAMSES*, which is to increase the maximum refinement level at fixed scale factor intervals to roughly maintain a constant maximum physical resolution, we keep the maximum refinement level fixed throughout the simulation. Hence the minimum physical cell widths are smaller at the start of the simulation than at $z = 6$. The difference in minimum cell size is not much different than at $z = 6$ though, since the maximum level is first triggered at $z \sim 20$ and thus the finest cells are ~ 3 times smaller (i.e. ~ 3.5 pc) than at $z = 6$.

The resolution of the gravitational force is the same as that of the gas, with the gravitational potential calculated for each cell. In the fiducial-resolution s05_256 and s10_512 runs, the DM density is smoothed to the second-finest levels, whereas in the high-resolution s05_512 runs, the DM density is applied to the finest level. This smoothing of the DM density is decided from analogue pure DM simulations using the refinement criteria stated above but without any limit in the maximum refinement. The maximum refinement actually reached in those pure DM simulations sets the maximum DM density level: ℓ_{max} for the high-resolution RHD simulations but $\ell_{\text{max}} - 1$ for the fiducial resolution.

2.4 Radiation

The methods for photon injection, M1 moment advection, and the interaction of radiation with hydrogen and helium gas via photoionization, heating, and direct radiation pressure, are fully described in Rosdahl et al. (2013). The radiation is split into three photon groups, bracketed by the ionization energies for H I, He I, and He II, and shown in Table 3. Radiation interacts with hydrogen and helium

via photoionization, heating, and momentum transfer (Rosdahl & Teyssier 2015). The group properties (average energies and cross sections to hydrogen and helium) are updated every 10 coarse time-steps from luminosity-weighted averages of the spectra of all stellar populations in the simulation volume, as described in Rosdahl et al. (2013). We do this so that at any time, the cross sections and photon energies are representative of the average photon population. Hence, as indicated in the Table 3 (and Fig. D1 in Appendix D), the energies and cross sections change by a few tens of per cent over the course of a simulation as the contributions from both old and metal-rich stellar populations increases.

In this work, we ignore the effects of radiation at subionizing energies (< 13.6 eV). We have run a subset of small-volume simulations at the fiducial resolution with added optical and reprocessed infrared radiation groups, and including multiscattering radiation pressure on dust as described in Rosdahl & Teyssier (2015) and Rosdahl et al. (2015), but found a negligible impact. This is likely because of the low metal and dust content at the early epoch we are concerned with.

Radiation is advected on the grid with an explicit solver, and therefore the simulation time-step is subject to the Courant condition. Since the RT time-step can become significantly smaller than the hydrodynamic time-step, we subcycle the RT on each AMR level, with a maximum of 500 RT steps performed after each hydro step (if the projected number of RT steps exceeds 500, the hydro time-step length is decreased accordingly). During the subcycling on each level, radiation is prevented from propagating to other levels and the radiation flux across boundaries is treated with Dirichlet boundary conditions; when advecting radiation on grid refinement level ℓ , the radiation density and flux in neighbouring cells at the finer ($\ell + 1$) and coarser ($\ell - 1$) levels is fixed at the states from the last RT steps performed at those levels. Radiation can cross boundaries *into* the level currently being subcycled, but to prevent ‘bursts’ of radiation across level boundaries, levels $\ell \pm 1$ are not updated when subcycling level ℓ ; these updates are performed only when those other levels are being RT subcycled. In this scheme, perfect photon conservation is not strictly maintained across level boundaries, although we have verified with tests that the number of photons is conserved to the level of a few per cent or less. For details of the same subcycling scheme in the context of flux-limited diffusion, see Commerçon, Debout & Teyssier (2014).

To prevent prohibitively small time-steps and a large number of RT subcycles, we use the variable speed of light approximation (VSLA) described in Katz et al. (2017), with a *local* speed of light $\tilde{c} = f_c c$ reduced by a factor f_c from the real speed of light c . Here, we apply a relatively slow speed of light in the finest grid cells, which typically represent the ISM of galaxies, and increase the speed of light by a factor 2 for every coarser level, up to a light speed fraction $f_c = 0.2$ in the coarsest cells. These correspond to diffuse voids in the simulation volume (to be precise, the coarsest cells all have density less than eight times the critical density). This naturally follows the velocity increase of ionization fronts with lower gas density (Rosdahl et al. 2013) and allows us to reduce the cost of the calculation by reducing the speed of light in the regions that constrain the global time step.

In our 10 cMpc volume, the speed of light fraction is set to $f_c = [0.2, 0.1, 0.05, 0.025, 0.0125]$ for refinement levels $\ell = [9, 10, 11, 12, 13]$, and is fixed at $f_c = 0.0125$ for $\ell \geq 13$. Even with the VSLA, using the full speed of light at the coarsest level(s) is prohibitively expensive. However, Katz et al. (2018) show that the reionization history is fairly well converged with this setup (see also Gnedin 2016). The main deviations are $\lesssim 10$ per cent overshoot in

Table 3. Photon group energy (frequency) intervals and properties. The energy intervals defined by the groups are indicated in units of eV by ϵ_0 and ϵ_1 and in units of Ångstrom by λ_0 and λ_1 . The last four columns show photon properties derived every 10 coarse time-steps from the stellar luminosity weighted SED model. These properties evolve over time as the stellar populations age, and the approximate variation is indicated in the column headers (the difference is similar in the two SED models we use in this work). $\bar{\epsilon}$ denotes the photon energies, while $\sigma_{\text{H I}}$, $\sigma_{\text{He I}}$, and $\sigma_{\text{He II}}$ denote the cross sections for ionization of hydrogen and helium, respectively.

Photon group	ϵ_0 (eV)	ϵ_1 (eV)	λ_0 (Å)	λ_1 (Å)	$\bar{\epsilon}$ (eV) ±20 per cent	$\sigma_{\text{H I}}$ (cm ²) ±10 per cent	$\sigma_{\text{He I}}$ (cm ²) ±10 per cent	$\sigma_{\text{He II}}$ (cm ²) ±25 per cent
UV _{H I}	13.6	24.59	9.1×10^2	5.0×10^2	18.3	3.2×10^{-18}	0	0
UV _{He I}	24.59	54.42	5.0×10^2	2.3×10^2	33.9	6.2×10^{-19}	4.7×10^{-18}	0
UV _{He II}	54.42	∞	2.3×10^2	0	63.3	9.3×10^{-20}	1.4×10^{-18}	1.2×10^{-18}

the volume-weighted neutral fraction, $Q_{\text{H II}}$, during the final stage of reionization, when voids are being ionized, and a few tens of per cent overshoot (undershoot) in the volume-weighted neutral fraction (photoionization rate) when the volume is completely reionized. For our comparison between SED models, these VLSA effects are negligible. Note that the variable speed of light conserves the total number of photons. The density of photons for group i , \mathcal{N}_i varies locally and inversely with the speed of light, but the flux, $\bar{c}\mathcal{N}_i$ remains exactly constant (see Rosdahl et al. 2013; Katz et al. 2017).

With our set-up for RT subcycling and the VSLA, the RT is rarely subcycled more than 10 times on any given level. The only exception to this occurs early on in the simulations when the first stars have just been born and are emitting ionizing photons but SN have yet to occur. In this case, the hydro time steps are still very long compared to the RT time steps.

2.4.1 Single and binary star radiation sources

In this work, we compare the stellar emission from two SED models; the GALAXEV model of Bruzual & Charlot (2003)³ and the Binary Population and Spectral Synthesis code (BPASS; Eldridge, Izzard & Tout 2007; Stanway et al. 2016).⁴ The latter includes binary stars while the former does not; for simplicity, we refer to the Bruzual & Charlot (2003) model as singles and the BPASS model as binaries throughout this paper.

For the single stars, we use the model generated with the semi-empirical BaSeL 3.1 stellar atmosphere library (Westera et al. 2002) and a Kroupa (2001) initial mass function (IMF). For the binaries, we use the available IMF closest to Kroupa (2001), with slopes of -1.3 from 0.1 to $0.5 M_{\odot}$ and -2.35 from 0.5 to $100 M_{\odot}$. In Appendix D, we describe in detail how we extract luminosities and photon group properties from the assumed SEDs, and show how the group properties evolve with age and metallicity.

Fig. 3 shows the instantaneous and integrated luminosities (\mathcal{L}_M and Π , respectively) for the two sets of SED models, for solar metallicity (Z_{\odot}) and $1/20 Z_{\odot}$, which is the lowest metallicity available in BPASS.⁵ There are two important differences to note. First, for low metallicity, the binaries model emits almost twice as many ionizing photons than the singles model. Secondly, at any metallicity, the ionizing luminosity decreases significantly faster with stellar age for the singles model compared to the binaries. For example, for $Z = 0.05 Z_{\odot}$, a singles population emits 86, 97, and 99 per cent of

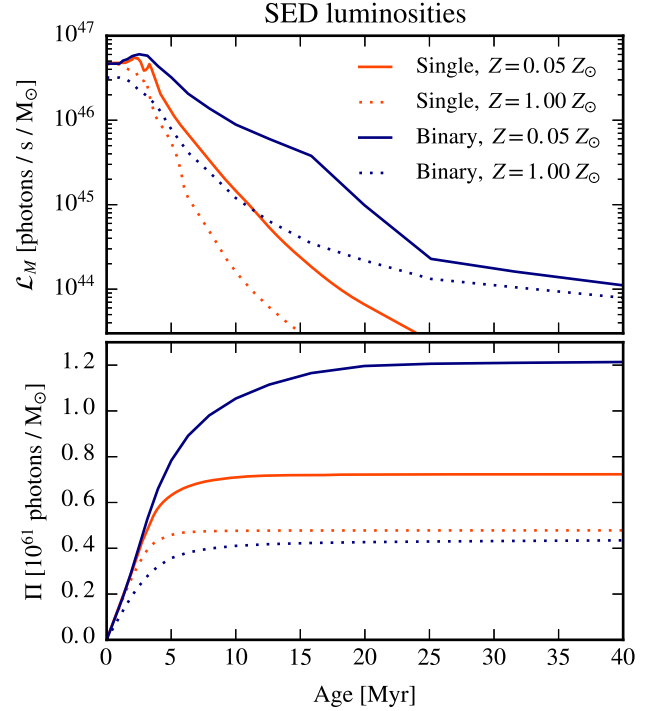


Figure 3. Ionizing luminosities (\mathcal{L}_M ; upper panel) and cumulative number of hydrogen-ionizing photons (Π ; lower panel) as a function of stellar population age for SED models with single stars only (Bruzual & Charlot 2003) in red and binary stars (Stanway et al. 2016) in blue. The solid curves are with solar metallicity and the dashed with $1/20$ th solar. At any metallicity, the luminosity decline is slower with binary stars included. At low metallicity, the inclusion of binary stars leads to almost twice as many ionizing photons as the case of single stars only.

its ionizing photons in the first 5, 10, and 15 Myr, respectively (the total is taken at 20 Gyr, where the model ends), while the binaries population has emitted only 63, 85, and 93 per cent of all its ionizing photons at the same ages.

Both differences may cause the binaries SED model to reionize the Universe earlier than the singles model. However, simply increasing the number of available photons by a small factor does not necessarily cause significantly earlier reionization, as the radii of ionization bubbles scale only as luminosity to the power of one-third (Strömgren 1939). The more prolonged emission with binaries is likely more important because what matters most is how many photons escape the dense ISM and penetrate out into the low-density IGM where only 1 photon per baryon is required to maintain ionization. Due to the interplay with stellar feedback, a stellar population is born in dense gas where the ionizing radiation is absorbed very efficiently in keeping up with the rapid rate of hydrogen recomba-

³www.bruzual.org/bc03/Updated_version_2016/BC03_base1_kroupa.tgz

⁴<http://bpass.auckland.ac.nz/2.html>

⁵For the Bruzual & Charlot (2003) model, we have used the interpolation scheme in RAMSES-RT to retrieve the low-metallicity curve and compare with BPASS, since the exact metallicity of $1/20$ th solar is not tabulated in the official distribution.

tions, but as the population gets older, feedback processes can clear away the gas, allowing ionizing radiation to escape into the IGM (Kimm & Cen 2014; Ma et al. 2016; Kimm et al. 2017; Trebitsch et al. 2017a).

2.4.2 Unresolved escape fractions

In previous simulations of reionization, the escape fraction of ionizing radiation on unresolved scales, f'_{esc} , is typically calibrated such that the injected radiation is either higher or lower than that given by the SED model used. A subunity f'_{esc} is then interpreted as modelling underresolved overdensities, correcting for underestimated recombination rates and too many photons escaping the unresolved region, while $f'_{\text{esc}} > 1$ models boost the luminosity of stellar sources to compensate for e.g. underresolved escape channels, underresolved turbulence (Safarzadeh & Scannapieco 2016), or secondary ionization from X-ray binaries (Shull & van Steenberg 1985). The calibration on f'_{esc} is usually done in such a way that the Universe is reionized at the roughly the correct redshift ($z \approx 10$ –6, depending on the definition of ‘reionized’), as determined from observations.

In this work, we do not perform calibration on unresolved escape fractions, always setting $f'_{\text{esc}} = 1$. This does not mean that we are sure to fully resolve the escape of ionizing radiation from sources deep within galaxies. However, since we are primarily interested in comparing reionization histories and escape fractions with two different SED models, and since we find that the two SED models result in reionization histories that bracket current observational constraints, there is no particular need for calibration. This non-essential calibration of f'_{esc} can be interpreted as either a balance between underresolved clumps and underresolved escape channels, or, more likely, an indication that the escape of radiation is governed more by large-scale feedback, captured with ~ 10 pc resolution, than the detailed turbulent motions of gas on pc and subpc scales.

2.5 Gas thermochemistry

The non-equilibrium hydrogen and helium thermochemistry, coupled with the local ionizing radiation, is performed with the quasi-implicit method described in Rosdahl et al. (2013) via photoionization, collisional ionization, collisional excitation, recombination, bremsstrahlung, homogeneous Compton cooling/heating off the cosmic microwave background, and di-electronic recombination. Along with the temperature, and photon fluxes, we track in every cell the ionization fractions of hydrogen, singly, and doubly ionized helium ($x_{\text{H II}}$, $x_{\text{He II}}$, $x_{\text{He III}}$, respectively), and advect them with the gas, like the metal mass fraction, as passive scalars. The thermochemistry is operator split from the advection of gas and radiation and performed with adaptive-time-step subcycling on every RT time-step (i.e. the thermochemistry is subcycled within the RT, which is subcycled within the hydrodynamics). To reduce the amount of thermochemistry subcycling, we use the ‘smoothing’ method for unsplitting the advection and injection of photons from the thermochemistry, described in Rosdahl et al. (2013). We assume the on-the-spot approximation, whereby we ignore recombination emission of ionizing photons, assuming it is all absorbed locally, within the same cell.

For $T > 10^4$ K, the cooling contribution from metals is computed using tables generated with CLOUDY (Ferland et al. 1998, version 6.02), assuming photoionization equilibrium with a Haardt & Madau (1996) UV background. The metal cooling is not currently modelled self-consistently with the local radiation, which is

a feature reserved for future work. For $T \leq 10^4$ K, we use the fine structure cooling rates from Rosen & Bregman (1995), allowing the gas to cool radiatively to a density-independent temperature floor of 15 K. We do not apply a density-dependent pressure floor to prevent numerical fragmentation: our SF model (see below) is designed to very efficiently form stars at high gas densities and, in unison with SN and radiation feedback, prevent overly high densities and numerical fragmentation.

2.6 Star formation

We use the turbulent SF criterion inspired by Federrath & Klessen (2012), as described in Kimm et al. (2017), Trebitsch et al. (2017a), and Devriendt (in preparation).

The following conditions must be met locally for stars to form in a cell.

(i) The local hydrogen density $n_{\text{H}} > 10 \text{ cm}^{-3}$ and the local overdensity is more than a factor 200 greater than the cosmological mean (the latter is needed to prevent ubiquitous SF at extremely high redshift).

(ii) The turbulent Jeans length is unresolved, i.e. $\lambda_{\text{J, turb}} < \Delta x$, where Δx is the finest cell width and the turbulent Jeans length is given by (Bonazzola et al. 1987; Federrath & Klessen 2012)

$$\lambda_{\text{J, turb}} = \frac{\pi \sigma_{\text{gas}}^2 + \sqrt{36\pi c_s^2 G \Delta x^2 \rho + \pi^2 \sigma_{\text{gas}}^4}}{6G\rho\Delta x}, \quad (2)$$

where σ_{gas} is the gas velocity dispersion over neighbour cells sharing vertices with the host.

(iii) The gas is locally convergent and at a local density maximum compared to the six next-neighbour cells.

Gas that satisfies the above criteria is converted into stellar population particles at a rate

$$\dot{\rho}_* = \epsilon_* \rho / t_{\text{ff}}, \quad (3)$$

where $t_{\text{ff}} = [3\pi/(32G\rho)]^{1/2}$ is the local free-fall time and ϵ_* is the SF efficiency. The cell gas is stochastically converted into collisionless stellar particles by sampling the Poisson probability distribution for gas to star conversion over the time-step (see Rasera & Teyssier 2006, for details), such that *on average*, the conversion rate follows equation (3). The initial mass of each stellar particle is an integer multiple of $m_* = 10^3 M_{\odot}$, but capped so that no more than 90 per cent of the gas is removed from the cell. The main distinction of this turbulent SF recipe from traditional SF in RAMSES (Rasera & Teyssier 2006), where ϵ_* is a global (typically small) constant, is that ϵ_* varies locally with the thermoturbulent properties of the gas (see Kimm et al. 2017; Trebitsch et al. 2017a; Devriendt, in preparation, for details). The local SF efficiency can approach and even exceed 100 per cent (with $\epsilon_* > 1$ meaning that stars are formed faster than in a free-fall time). This gives rise to a bursty mode of SF, whereas the classical constant ϵ_* recipe leads to SF that is more smoothly distributed in both space and time.

We modify the SF recipe as described by Kimm et al. (2017) by subtracting rotational velocities and symmetric divergence from the turbulent velocity dispersion in equation (2) and the expression leading to ϵ_* , such that the turbulence represents only anisotropic and unordered motion. This leads to stronger instantaneous SF at the centres of galaxies and rotating clouds, but also stronger feedback episodes, with the net effect of reducing the overall SF.

2.7 Supernova feedback

We apply individual Type II SN explosions of 10^{51} erg by stochastically sampling the delay-time distribution for the IMF over the first 50 Myr of the lifetime of each stellar particle.

We use the mechanical SN model for momentum injection from Kimm et al. (2015, see also Kimm et al. 2016, 2017; Rosdahl et al. 2017; Trebitsch et al. 2017a, and a similar model described in Hopkins et al. 2014). The key feature of the mechanical feedback model is its ability to capture the correct final snow-plow momentum of an SN remnant, by injecting it directly if the previous adiabatic phase is not resolved, or otherwise letting it evolve naturally. We review here the main features of the algorithm.

For one SN explosion, its radial momentum, along with the SN ejecta mass (m_{SN}), as well as gas mass contained in the host SN cell, is shared between the host and all neighbour cells sharing vertices with it (corners included; thermal energy is injected into the host instead of momentum). The amount of momentum given to each neighbour depends on the mass loading $\chi = \Delta m_{\text{W}} / (f_{\text{nbor}} m_{\text{SN}})$. Here, the denominator is the SN ejecta mass received by the neighbour, with f_{nbor} a geometrical factor determining the share of SN energy and mass that the neighbour receives (totalling to unity for each explosion). The numerator, Δm_{W} , contains all the mass in the same neighbour after the wind injection (i.e. the mass already in the cell plus the SN remnant plus f_{nbor} times the mass originally in the SN host cell).

For low χ , the momentum injection follows the adiabatic phase with

$$\Delta p = f_{\text{nbor}} \sqrt{2\chi m_{\text{SN}} f_e E_{\text{SN}}}. \quad (4)$$

Here, f_e is a function ensuring a smooth transition to the maximum momentum injection for the neighbour,

$$\Delta p_{\text{max}} = 3 \times 10^5 M_{\odot} \frac{\text{km}}{\text{s}} E_{51}^{16} n_0^{-\frac{2}{17}} Z'^{-0.14} f_{\text{nbor}}, \quad (5)$$

where E_{51} is the SN energy in units of 10^{51} erg and always unity in these simulations, n_0 is the local hydrogen number density in units of 1 cm^{-3} , and $Z' = \max(Z/Z_{\odot}, 0.01)$. This expression for the density- and metallicity-dependent upper limit for the snowplow momentum comes from the numerical experiments of Blondin et al. (1998) and Thornton et al. (1998) of explosions in a homogeneous medium and has been confirmed more recently by e.g. Kim & Ostriker (2015) and Martizzi, Faucher-Giguère & Quataert (2015).

As in Kimm et al. (2017), we increase the maximum injected momentum in cells where ionized (H II) regions are unresolved. At each SN injection, we compare the local Strömgren radius r_{S} (Strömgren 1939) with the cell width Δx . Based on a simple fit to the results of Geen et al. (2015), for $r_{\text{S}} > \Delta x$, the magnitude of the injected momentum gradually shifts to

$$\Delta p_{\text{max}}^{\text{PH}} = 4.2 \times 10^5 M_{\odot} \frac{\text{km}}{\text{s}} E_{51}^{16} Z'^{-0.14} f_{\text{nbor}}, \quad (6)$$

due to the unresolved clearing of dense gas via photoionization heating.

We assume a Kroupa (2001) IMF, where a mass fraction $\eta_{\text{SN}} = 0.2$ of the initial stellar population mass explodes as SNe and recycles back into the ISM with a metal yield of $y = 0.075$ (i.e. 7.5 per cent of the ejecta hydrogen plus helium mass is converted to heavy elements). Integration of the Kroupa IMF to $100 M_{\odot}$ gives an average SN progenitor mass of $m_{\text{SN}} = 20 M_{\odot}$, resulting in $\eta_{\text{SN}}/m_{\text{SN}} = 1$ SN explosion per 100 solar masses. However, we calibrate the SN feedback in order to roughly reproduce the early Universe stellar mass to halo mass (SMHM) relation, SFR versus halo mass,

and UV luminosity function (these plots are shown in Section 3.1 and the effects of the calibration are detailed in Appendix C). As a result, the SN rate is boosted by assuming $m_{\text{SN}} = 5 M_{\odot}$, which gives four SN explosions per 100 solar masses, four times higher than the Kroupa IMF.

The boost in the rate of SN explosions is pure calibration, but can be viewed as representing uncertain factors of: (i) the high-mass end of the IMF (a less conservative integration over 6–150 M_{\odot} gives an SN rate close to ours), (ii) numerical overcooling (Katz, Weinberg & Hernquist 1996),⁶ and (iii) complementary feedback processes such as cosmic rays (e.g. Booth et al. 2013; Hanasz et al. 2013; Girichidis et al. 2016; Pakmor et al. 2016), stellar winds (e.g. Gatto et al. 2016), and radiation pressure in the Lyman-alpha (Dijkstra & Loeb 2009; Smith, Bromm & Loeb 2016; Kimm et al. 2018) and infrared (e.g. Thompson, Quataert & Murray 2005; Hopkins, Quataert & Murray 2012, but see Rosdahl et al. 2015).

We make no SED-dependent adjustments to the SN feedback. In reality, the rate of SN explosions is inherently tied to the SED model: for example, mass transfer between binary companions leads to an increased number of Type II SN explosions for a stellar population, and at later times. However, to minimize the number of variables in our comparison between SED models, we ignore these factors in the present study.

3 RESULTS

We first demonstrate the range of scales captured in our cosmological simulations. In Fig. 4, we show maps of hydrogen column densities (N_{H}) in the 10 cMpc volume (run with binary stars) at $z = 6$, starting in the top-left panel with a projection of the full volume, then clockwise showing the large-scale environment of the most massive halo, and a zoom-in on the halo gas. The insets in the bottom-left panel show zoom-ins on the central galaxy of N_{H} , stellar column density (Σ_{*}), hydrogen photoionization rate ($\Gamma_{\text{H II}}$), and ionized hydrogen fraction ($x_{\text{H II}}$). The images show clear signatures of violent feedback events and outflows, mergers, and accretion, with expanding remnants of SN superbubbles (top-right panel of halo environment) and a generally unsettled morphology of gas.

The photoionization rate is a measure for the flux of ionizing radiation and is calculated as

$$\Gamma_{\text{H II}} = \sum_{i=1}^{N_{\text{groups}}} \tilde{c} \mathcal{N}_i \sigma_{i, \text{H II}}, \quad (7)$$

where \tilde{c} is the local reduced speed of light, N_{groups} is the number of radiation groups, \mathcal{N}_i is the photon number density for radiation group i , and $\sigma_{i, \text{H II}}$ is the hydrogen photoionization cross section for group i . The map of $\Gamma_{\text{H II}}$ in Fig. 4 shows that the ionizing radiation emitted by some stellar populations is efficiently absorbed by the ISM, for example inside the central bulge where there is a bright spot of high photoionization rate, at the location of a young cluster of stars, surrounded by a darker region of relatively low $\Gamma_{\text{H II}}$ and high neutral gas density. In other regions, for example north-east from the central bulge, the radiation propagates much more freely through, and away from, the ISM.

We now compare our galaxy populations to observables of the high-redshift Universe and demonstrate that we reproduce an accurate luminosity budget for our simulated patches of the Universe.

⁶The Kimm et al. (2015) subgrid model circumvents numerical overcooling of SN blasts by design, but even so overcooling may still be an issue, e.g. due to underresolved gas porosity (Kimm et al. 2015).

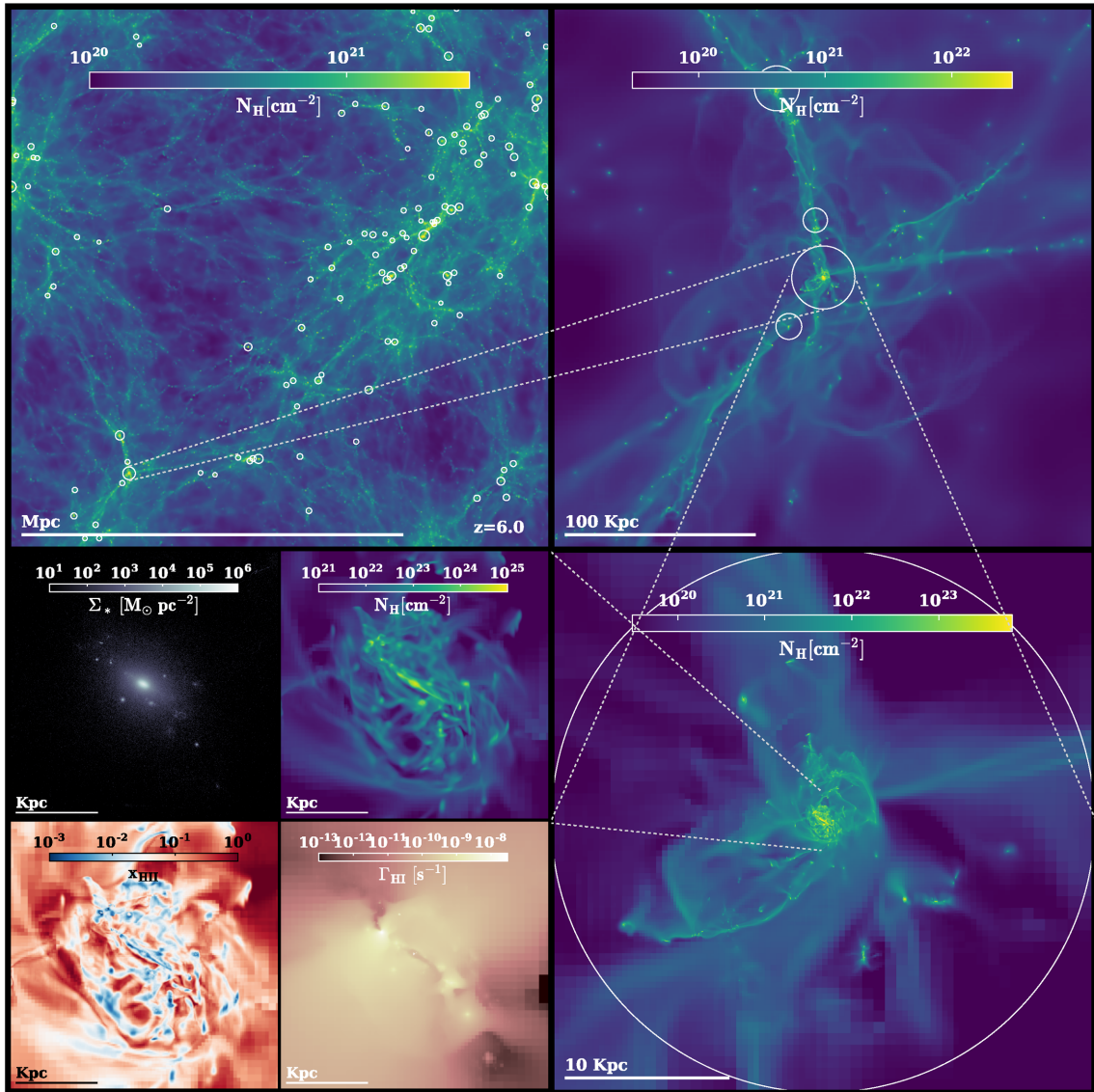


Figure 4. Projections from the 10 cMpc volume at $z = 6$, run with binary stars (s10_512_BINARY). Circles mark the virial radii of all haloes more massive than $3 \times 10^9 M_{\odot}$. Clockwise from top left, the first three panels show hydrogen column densities, N_{H} , first for the full volume, then in the environment around the most massive halo ($M_{\text{vir}} = 4.7 \times 10^{10} M_{\odot}$), and finally inside that halo. The four subpanels in the bottom-left corner zoom in on the central galaxy and show, clockwise from top right, the column density of gas, averaged hydrogen photoionization rate, Γ_{HII} , average density-weighted ionized hydrogen fraction, x_{HII} , and stellar column density, Σ_{*} .

We will then present our simulated reionization histories, and finish by comparing the redshift-evolution of escape fractions with single and binary SED models.

3.1 Galaxy properties

We begin with the $z = 6$ SMHM relation. We assign to each halo the most massive galaxy within $0.3 R_{\text{vir}}$ (as identified by ADAPTAHOP). The resulting SMHM relation is shown in Fig. 5 for the 10 cMpc volumes with binary and single SED models. We have binned the haloes by mass and plotted the mean stellar mass per bin, with the sizes of circles indicating the number of galaxies per bin, and shaded areas showing the standard deviation. We note that our 5 cMpc volume results are very similar to those for the 10 cMpc one, only extending to lower maximum (and minimum) halo masses.

The different SED models produce similar SMHM relations. This is due to the fact that, except for the SED models, we use the exact same parameters and SN feedback model in those runs, underlining that stellar mass is mostly regulated by SNe in our simulations. There is secondary feedback via photoionization heating (Rosdahl et al. 2015) that leads to the SMHM relation in Fig. 5 being shifted down by ~ 25 per cent with the binary stars SED model compared to the singles case. An identical run without any ionizing radiation (not shown) results in an SMHM relation that is shifted up by ~ 40 per cent compared to the single-stars SED model. We stress though that the photoionization feedback is subdominant compared to SNe, which have a much more dramatic effect on the stellar mass (see Appendix C and in particular Fig. C2 for the effect of SN feedback).

We compare our SMHM relation in Fig. 5 to find estimates from rotation curves of $z = 0$ dwarf galaxies (Read et al. 2017, for lack of direct observational constraints with such low-mass haloes at high

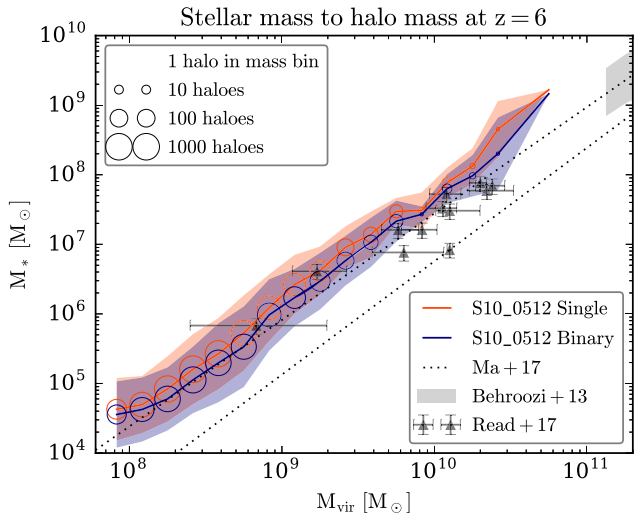


Figure 5. SMHM relation in out 10 cMpc volume at $z = 6$. The red and blue curves show average stellar masses per halo mass bins for the single and binary SED models, respectively, with circle sizes representing the number of galaxies in each bin, as indicated in the top left legend, and shaded regions marking the standard deviation. The grey shaded area in the top-right corner shows observational $z = 6$ constraints from abundance matching (Behroozi, Wechsler & Conroy 2013) and black triangles show observational constraints of $z = 0$ isolated dwarf galaxies (Read et al. 2017). The dashed curves represent the 1σ dispersion in the simulations of Ma et al. (2018). The simulated galaxies are in fair agreement with the Ma et al. (2018) simulations as well as $z = 0$ observations.

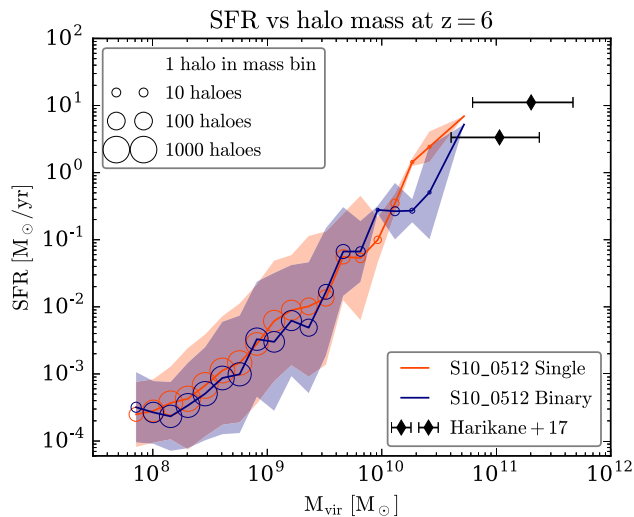


Figure 6. SFR, averaged over the last 100 Myr, versus halo mass for our 10 cMpc simulations with single (red) and binary (blue) SED models. The curves indicate mean SFRs in each halo mass bin and the shaded regions show the standard deviation. Circle sizes represent the number of galaxies per halo mass bin. Diamonds show observational $z = 6$ estimates from Harikane et al. (2018). The simulated galaxies show a large scatter in SFRs and a fair agreement with the observational estimates, although the overlap is limited.

redshift), with which our simulations are in good agreement, and $z = 6$ observational constraints from abundance matching (Behroozi et al. 2013) which, while not overlapping with our mass range, are not in obvious conflict with our results. The figure also includes predictions from the cosmological EoR simulations of Ma et al.

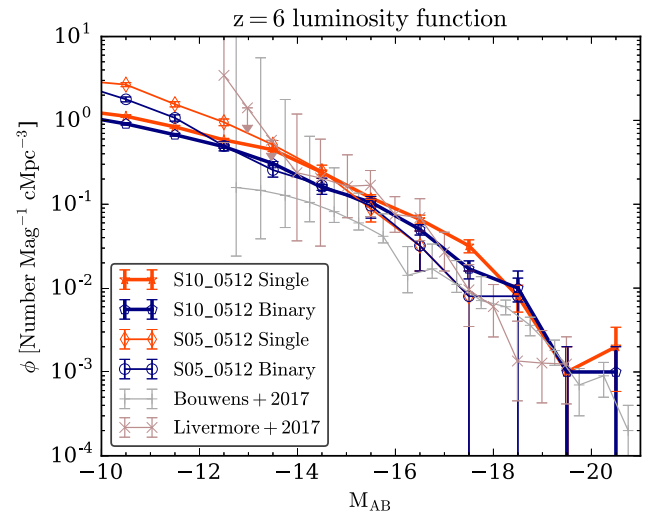


Figure 7. Redshift 6 luminosity functions from our 10 and higher resolution 5 cMpc volumes (ignoring absorption), and from the observational compilations of Bouwens et al. (2017) and Livermore, Finkelstein & Lotz (2017), as indicated in the legend. We use Poissonian error bars for the SPHINX data, but note that the error from cosmic variance is typically larger. Our simulations agree well with the observational limits. Systematically more galaxies appear at the low-luminosity end with the single-stars SED.

(2018), with dashed lines marking their 1σ scatter in galaxy masses. Our galaxy masses are slightly but systematically higher than theirs, which is very likely due to less efficient stellar feedback, but the SMHM relation is very similar in slope. Our scatter in galaxy mass is similar to theirs at all masses; much like them we find that the scatter in stellar masses decreases somewhat towards the high-mass end, but for halo masses $\gtrsim 10^{10} M_{\odot}$, our relative lack of scatter is merely a result of limited statistics, with only a few haloes populating this regime (see Fig. 2).

In Fig. 6, we show the mean SFRs averaged over the past 100 Myr as a function of halo mass at $z = 6$. Again, there is little overlap with $z = 6$ observations except at the very highest masses of our simulated haloes. For comparison, we include estimates from Harikane et al. (2018), with which our highest mass galaxies are in reasonable agreement. Again, there is slightly but systematically lower SF efficiency with the binary SED, hinting at non-negligible effects from the more luminous and prolonged radiation emitted from binary stellar populations, compared with the single-stars SED.

To generate luminosity functions from our simulation outputs, we sum the 1500 \AA luminosities of all stellar particles in each galaxy (as identified by ADAPTAHOP). The luminosity of each stellar particle is calculated by interpolating tables of metallicity- and age-dependent 1500 \AA luminosities for each SED. We transform the total 1500 \AA luminosity, L_{1500} , of each galaxy to an absolute AB magnitude (Oke & Gunn 1983),

$$\begin{aligned} M_{\text{AB}} &= -48.6 - 2.5 \log \left(\frac{L_{1500} / [\text{erg s}^{-1} \text{ Hz}]}{4\pi [10 \text{ pc/cm}]^2} \right) \\ &= 51.595 - 2.5 \log \left(\frac{L_{1500}}{\text{erg s}^{-1} \text{ Hz}} \right). \end{aligned} \quad (8)$$

We ignore dust absorption, which is predicted by Ma et al. (2018) to become important at $z \sim 6$ for intrinsic magnitudes $M_{\text{AB}} \sim -20$ and brighter.

The resulting luminosity functions are plotted in Fig. 7 and compared to observations from Bouwens et al. (2017) and Livermore et al. (2017). The overall agreement with observations is good, in-

dicating that we produce a realistic number of photons over the range of halo masses captured in our simulations. Thus, our results are not compromised by an over-abundance or underabundance of galaxies at a given luminosity. We note that including an absorption of ≈ 0.5 mag at the bright end (as suggested e.g. by Ma et al. 2018 or Bouwens et al. 2015) would further improve the agreement of our results with observations. It should also be noted that our statistics at the luminous end are very limited, with the most luminous bins in each of our volumes containing only 1–2 galaxies. For future comparisons, we tabulate our predicted luminosity functions with the binary SED, at $z = 10, 8,$ and $6,$ in Appendix A.

At the faint end, for $M_{\text{AB}} \gtrsim -13,$ discrepancies appear for the box sizes, with a systematically larger number of faint galaxies for the 5 cMpc volume than for the 10 cMpc volume (this is true both for the single and binary SED models, though the discrepancy appears in slightly brighter galaxies with single stars). The discrepancies are due to the different cosmological ICs (and not to differences in resolution: luminosity functions for the 5 cMpc box with varying resolution are much better converged, as shown in Appendix B).

Overall, due to strong calibrated SN feedback, our simulated volumes contain galaxies that are in good agreement with observations in terms of stellar masses, SFRs, and luminosity functions. Hence, the simulated production of ionizing photons per volume should roughly match the real production of photons over the range of halo masses represented in our simulations, assuming the SED models are accurate.

3.2 Reionization history

We now turn to the reionization histories produced in our volumes with single and binary SED models. Fig. 8 shows a visual comparison of the volume for the two SED models, with single stars in the upper set of panels and binaries in the lower ones. The maps show projected distributions through the simulated volume of density-weighted gas temperature T (upper rows) and density-weighted hydrogen photoionization rate Γ_{HII} (lower rows) at redshifts 10, 8, and 6 (from left to right). The qualitative extent of ionized regions can be judged from the temperature projections, where deep blue marks cold neutral regions, light-blue to light-red shows photoionized gas, and darker red indicates gas that has been heated by SNe and, to a lesser extent, virial shocks. Comparing the upper and lower set of panels, it is clear that the IGM is ionized sooner and to a greater extent with binary stars included. At all redshifts shown, the ionized regions are much larger with binary stars and at $z = 6$ the individual H II bubbles have merged. Without binaries, there is still a significant fraction of the volume that remains neutral and with photoionization rates far below the $z \approx 6$ observational estimates of a few times 10^{-12} s^{-1} (Calverley et al. 2010; Wyithe & Bolton 2010; D’Aloisio et al. 2018).

Fig. 9 shows the redshift evolution of the volume-filling fraction of neutral hydrogen, Q_{HII} , for the 10 and 5 cMpc wide volumes, with single and binary SED models. Black datapoints in the same plot show model-dependent observational estimates from Fan et al. (2006), Schroeder et al. (2012), Ouchi et al. (2017), Sobacchi & Mesinger (2015), Inoue et al. (2018), and Bañados et al. (2018). The single and binary SED models produce very different reionization histories. The volumes are only ~ 50 per cent reionized at $z = 6$ with the single-stars SED, while they are completely reionized by $z \approx 7$ with binaries included. Note that for each SED, the two different curves are not only for different volume sizes (and hence a different range of halo masses) but also for different DM mass resolution, so the results are robust to both these factors. In Ap-

pendix B, we also show that these reionization histories are robust with respect to resolution only (i.e. not changing the volume size at the same time). This insensitivity to box size is in part due to our method for selecting ICs to minimize cosmic variance effects (see Section 2.2.1). It is also an indication that our volumes are mostly ionized by intermediate-mass haloes, i.e. in the mass range $M_{\text{vir}} \approx 10^8\text{--}10^{10} M_{\odot},$ since this is the mass range overlapping our two volumes (see Fig. 2).

Neither SED model produces a reionization history in perfect agreement with the observational limits, but it is compelling and reassuring that variations in state-of-the-art SED modelling produce reionization histories that bracket the observational limits, without any calibration in unresolved escape fractions.

Note that in order to produce the good agreement with observations of the SMHM, SFR to halo mass, and luminosity function, we artificially boost the rate of SN explosions by a factor of 4 compared to that derived from a Kroupa (2001) IMF. Without the factor 4 boost, our stellar masses and SFRs are systematically higher than observations by factors of a few, as shown in Appendix C. Likewise, the resulting luminosity function is far too shallow compared to observations. However, as we also show in Appendix C, our main results are surprisingly insensitive to the feedback calibration, with remarkably similar reionization histories produced with and without the SN boost, even if galaxy luminosities are vastly overestimated in the unboosted SN case.

In Fig. 10, we plot the simulated redshift evolution of the volume averaged Γ_{HII} in ionized gas, selecting only cells with hydrogen ionized fraction $x_{\text{HII}} > 0.5.$ The photoionization rate fluctuates strongly at high redshift, due to the rates being extracted from a small number of ionized regions nearby or inside haloes. Thus, Γ_{HII} is very sensitive to the current SFR. Some such regions, dim yet ionized by previous SF events, can easily be identified by matching the temperature and photoionization rate projections in Fig. 8. Over time, the number of ionized regions increases and the strength of the fluctuations decreases as the average becomes less sensitive to individual regions. Eventually, the fluctuations disappear completely with binary stars as individual H II bubbles merge and the radiation field in any location becomes a composite of all the sources in the volume. The photoionization rate slightly overpredicts observations at $z = 6$ although this is expected since the box reionizes at a marginally higher redshift than observations suggest. For the single-stars SED, the fluctuations remain until $z = 6,$ since the volume is not fully reionized, and the average photoionization rate is clearly well below the observational estimates, as expected from the reionization history in Fig. 9.

We finally note that our use of the variable reduced speed of light leads to a few tens of percent (relative) overpredictions of the neutral fraction and underpredictions of the photoionization rate, compared to a full light speed, when the volume is fully ionized (see Section 2.4 and a full explanation in Ocvirk et al. 2018; when reionization is completed and the whole volume becomes optically thin, the photon density turns light-speed independent and hence both the photon flux and the photoionization rate become light-speed dependent). With the binary SED model, a full speed of light would thus bring us further away from the $z \approx 6$ observational data in Figs 9 and 10.

3.3 Escape fractions for individual haloes

The VSLA makes it difficult to estimate f_{esc} directly from the M1 radiation field due to the different and untraceable delay times for photons to travel from their sources to a given distance. Therefore,

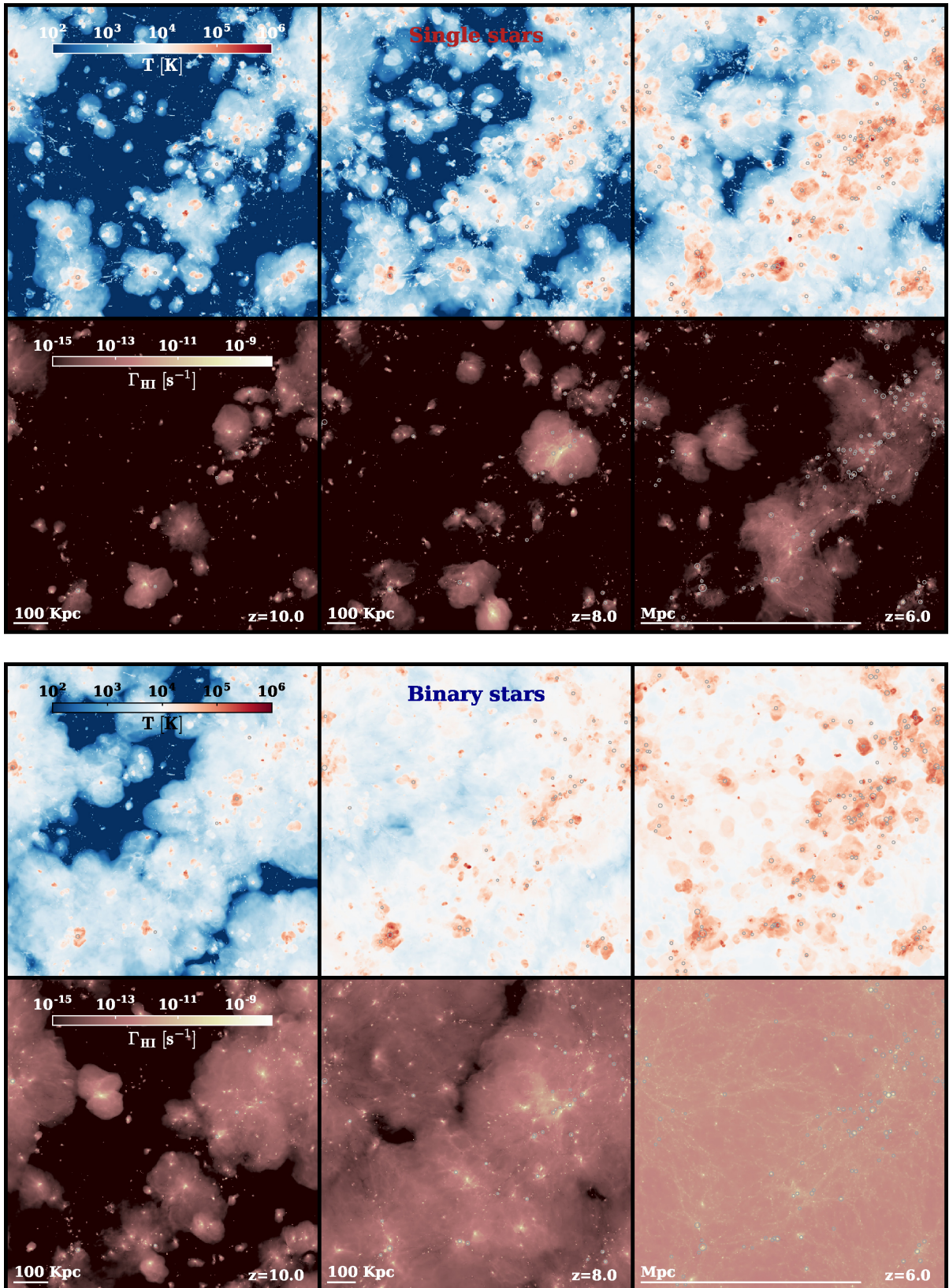


Figure 8. Reionization of the 10 cMpc volume with single and binary SED models (upper and lower set of panels, respectively). Each set of panels shows full volume mass-weighted projections of temperature (upper rows) and photoionization rate Γ_{HII} (lower rows) at decreasing redshift as indicated in the Γ_{HII} -maps. The circles mark all haloes more massive than $3 \times 10^9 M_{\odot}$. In the temperature maps, the blue colour shows cold neutral gas, white to reddish depicts warm photoionized gas, and darker red indicates gas shock-heated by galactic winds. By comparing the upper and lower set of panels, it is clear that the inclusion of binary stars (in the lower set of panels) hastens the reionization process.

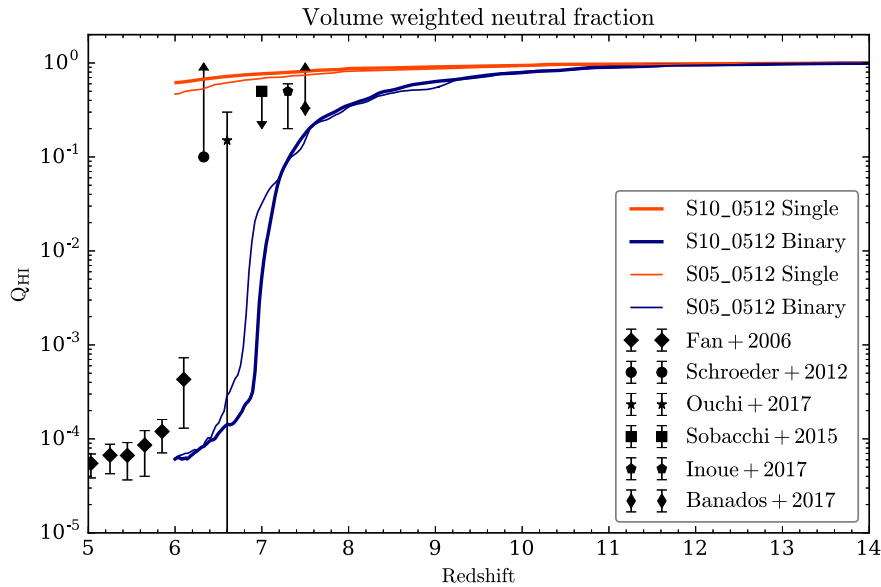


Figure 9. Evolution with redshift of the volume-filling neutral fraction, Q_{HII} . Our 10 and (higher DM–mass resolution) 5 cMpc volumes are shown, each with both single and binary SED models, as indicated in the legend. For comparison, we show model-dependent observational estimates from Fan, Carilli & Keating (2006), Schroeder, Mesinger & Haiman (2012), Ouchi et al. (2017), Sobacchi & Mesinger (2015), Inoue et al. (2018), and Bañados et al. (2018), as indicated in the legend. Changing the volume size and/or resolution has very little effect on the reionization history, whereas changing to an SED that includes binary stars dramatically hastens reionization.

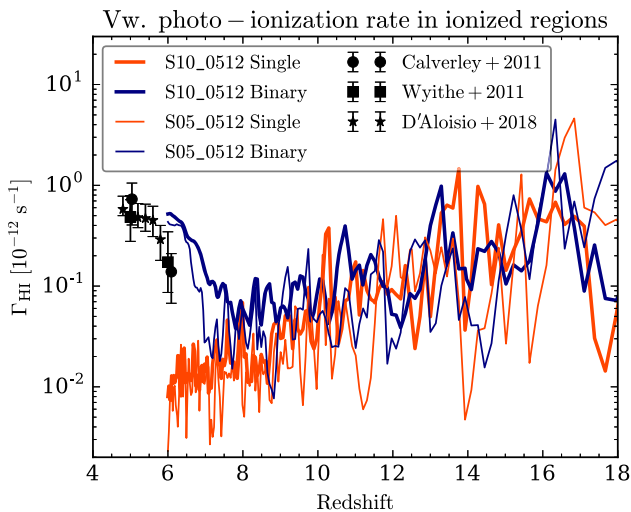


Figure 10. Redshift evolution of volume-weighted photoionization rate inside ionized regions ($x_{\text{HII}} > 0.5$) in our volumes. For comparison, we show observational estimates from Calverley et al. (2010), Wyithe & Bolton (2010), and D’Aloisio et al. (2018), as indicated in the legend. The rate fluctuates strongly during the process of reionization but these fluctuations diminish as the volume becomes fully ionized in the binary star simulations. This model overshoots observations slightly due to early reionization.

we measure the instantaneous escape fractions in post-processing by tracing rays from all stellar sources. We calculate the optical depth to neutral hydrogen and helium, τ , along each ray until it exits the virial boundary of its parent halo. We then determine the escape fraction for the ray as $e^{-\tau}$. The net escape fraction from each stellar particle is then the average of 500 rays with random directions, and the net escape fraction for a halo at a given time is the luminosity-weighted average for all stellar particles assigned to the halo. We assign each stellar particle to the closest (sub)halo,

using for each halo the weighted distance measurement $d = r/R_{\text{vir}}$, where r is the distance of the star from the halo centre. A star outside R_{vir} of any halo is not assigned and we do not assign to any subhalo fully enclosed within R_{vir} of its parent halo (i.e. stars within such a subhalo are assigned to its parent halo).

We have checked in a few outputs that casting 2000 rays per source gives relative differences in f_{esc} of less than 0.1 percent, compared to the fiducial 500 rays. Hence, it is fully justified to use 500 rays per source. Trebitsch et al. (2017a) showed that this method of tracing rays in post-processing yields almost identical results as integrating the flux of M1 photons across the virial radius (with a constant light-speed) and comparing to the galaxy’s ionizing photon production rate. Note that all of our escape fractions are luminosity-weighted, meaning f_{esc} represents the *average escape probability per ionizing photon*, not per source.

In Fig. 11, we compare the variation over time of f_{esc} from the most massive progenitor to the most massive halo at $z = 6$ ($M_{\text{vir}} \approx 10^{10} M_{\odot}$, $M_{*} \approx 10^8 M_{\odot}$) in the smaller volume s05_512 simulations, with single and binary SED models (in red and blue, respectively). As found by Kimm & Cen (2014), Wise et al. (2014), Ma et al. (2016) and Trebitsch et al. (2017a), the escape fraction varies strongly with time, due to regulation by SN feedback. Peaks in f_{esc} typically follow peaks in ionizing luminosity (denoted by thin curves) from bursty SF events. The highly fluctuating nature of f_{esc} makes it difficult to compare the binary and stellar SED models for a single halo, but the plot shows generally higher f_{esc} for the binary SED, especially at late times.

To demonstrate how the variation is regulated by feedback, Fig. 12 shows neutral hydrogen column density and photoionization rate projections for the binary SED model at the three times, indicated by thin vertical lines at 805–855 Myr in Fig. 11 (at this time, the virial mass of the halo is $10^{10} M_{\odot}$). The left-hand column corresponds to a peak of intrinsic ionizing luminosity, due to an ongoing starburst. The ISM of the galaxy is already quite disrupted but still intact enough that little of the ionizing radiation produced

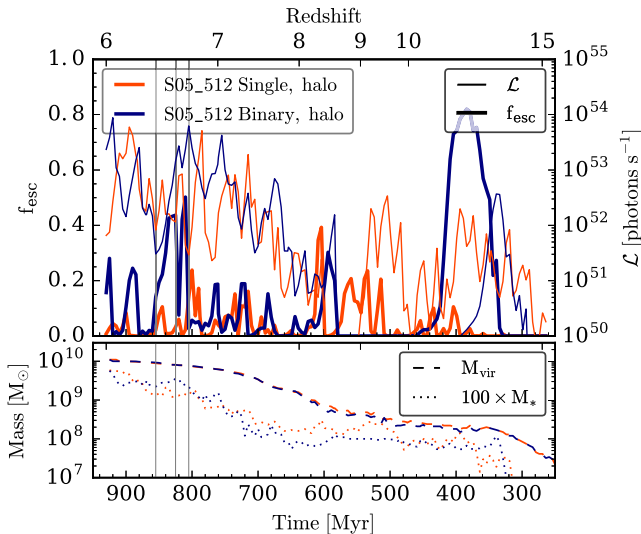


Figure 11. Variations over time in the escape of ionizing radiation, f_{esc} (thick solid curves), and intrinsic ionizing luminosity, \mathcal{L} (thin solid curves), for the most massive halo in the high-resolution 5 cMpc volume simulations. The red curves are with the single-stars SED and the blue curves are with binary stars included. In the lower panel, we show the corresponding evolution in the virial halo mass (dashed curves) and (one-hundred times the) stellar mass, identified as in Section 3.1. (Decreases in stellar mass are in part due to mass ejected in SN feedback, but more predominantly reflect the challenging identification of individual galaxies and their assignment to haloes, which is especially difficult in the merger-rich high-redshift Universe.) Thin vertical solid lines mark times corresponding to the halo images in Fig. 12. Both f_{esc} and the production of ionizing radiation vary enormously over time, due to feedback regulation.

can escape. In the middle column, SN explosions have disrupted the ISM to the extent that SF, and hence also the ionizing luminosity, is declining fast, but the more diffuse ISM now allows a significant fraction ($f_{\text{esc}} = 44$ per cent) of the ionizing photons to break out of the halo. In the right-hand column, not much ionizing radiation comes from the galaxy because (i) the ISM has settled back and f_{esc} is very low again and (ii) the galaxy has become very faint in ionizing radiation due to the drop in SF. This is a rather extreme example compared to most other peaks of f_{esc} in Fig. 11, but the picture is usually the same, with flashes of escaping ionizing radiation following SF (and subsequent feedback) events. The first such event for the binary case in Fig. 11, at time ≈ 400 Myr, is also the most extreme one in terms of duration and the peak value in f_{esc} . This is because, at this point, the system is very low in mass ($M_{\text{vir}} \approx 10^8 M_{\odot}$) and highly susceptible to disruption by SN feedback. This first strong starburst results in total obliteration of the ISM, so it takes more than a hundred million years to recover and start forming stars again.

3.4 Global escape fractions

Fig. 13 shows the global luminosity-weighted f_{esc} for the 10 cMpc volume, again for both the single and binary SED models, as well as the ionizing luminosities per volume (\mathcal{L}). We use the same definition for escape as in the previous section. We remind that we do not assign particles outside the R_{vir} of any halo, but note that such unassigned stellar particles account for less than 0.01 per cent of the total ionizing luminosity and hence their inclusion would have no effect on our estimated escape fractions.

Since the escape fraction is now averaged over a few thousand galactic sources, the fluctuations are not as extreme as seen in individual haloes, except at high redshift, when f_{esc} is dominated by a small number of galaxies. This makes it easier to compare the single- and binary-star SED models. In order to make the comparison even clearer, we plot in dotted curves the \mathcal{L} -weighted average over the last 100 Myr, or $f_{\text{esc}, 100}$. We show also the luminosity-weighted variance in the instantaneous f_{esc} , which is indicated with shaded regions. Note the distribution is highly non-Gaussian and the variance here is meant only to give an indication of the range in f_{esc} that we measure at a given redshift.

For the binary SED model, the global escape fraction is at $f_{\text{esc}} \approx 7$ –10 per cent for $z < 9$, while for the single-star SED model it is at $f_{\text{esc}} \approx 2$ –4 per cent. In both cases, there is a slight overall decline in f_{esc} with decreasing redshift. Sampled over every 5 Myr until $z = 6$, the \mathcal{L} -weighted average f_{esc} is 8.5 per cent for binaries and 2.7 per cent for singles (i.e. ≈ 3.1 times higher for binaries). This is in good agreement with Ma et al. (2016), who predict a factor of 3–6 boost in ‘true’ escape fractions (i.e. omitting an extra luminosity boost) with binaries.

The higher f_{esc} with binaries partially explains the much more efficient reionization with the binary SED model. However, as shown with thin curves in Fig. 13, the production rate per volume of ionizing photons, \mathcal{L} , is also somewhat higher for the binary SED model. It is the combination of higher escape fractions and higher ionizing luminosities that leads to earlier reionization with binary stars. However, since the ratio of escape fractions between the single and binary SED models (a factor few) is consistently and significantly higher than the ratio of luminosities for those same models (typically a few tens of per cent), we can conclude, as did Ma et al. (2016), that the higher f_{esc} dominates over the higher integrated luminosity with binary stars (seen in the lower panel of Fig. 3).

We further examine the variation in f_{esc} in Fig. 14, where we plot the luminosity-weighted probability distribution of escape fractions from all (halo-assigned) stellar particles at selected redshifts in our 10 cMpc wide volume, with binary and single stars. The distribution peaks at zero or near-zero f_{esc} , as expected, but for higher f_{esc} there are a few non-systematic bumps in each snapshot. The reason for these bumps is that a few galaxies in each snapshot exist in the luminous and optically thin phase (similar to the middle column in Fig. 12). In this phase, the majority of young stars are exposed to the same low column density channels where a fixed fraction of the ionizing radiation can escape. In contrast, other stars are embedded in high-density regions with negligible escape fractions (see also Cen & Kimm 2015; Trebitsch et al. 2017a). Such a galaxy typically has a bi-modal distribution in f_{esc} : we include an example of this in the light-blue curve in Fig. 14, which shows the f_{esc} distribution from the massive halo in the s05_512_BINARY simulation at a time of high f_{esc} (corresponding to the blue peak at ≈ 595 Myr in Fig. 11). The series of bumps in Fig. 14 represent the rare luminous galaxies with high f_{esc} , each having a bi-modal f_{esc} distribution, while most galaxies at a given time either have a low f_{esc} and contribute mostly to the peak at $f_{\text{esc}} \approx 0$, or they have a low luminosity and hence contribute little to the luminosity-weighted distributions plotted in Fig. 14. With larger simulation volumes, these bumps would presumably merge into a smooth distribution with a single peak at $f_{\text{esc}} = 0$.

4 DISCUSSION

With the SPHINX simulations, we find a significant boost in escape fractions with an SED model that includes binary stars, increasing

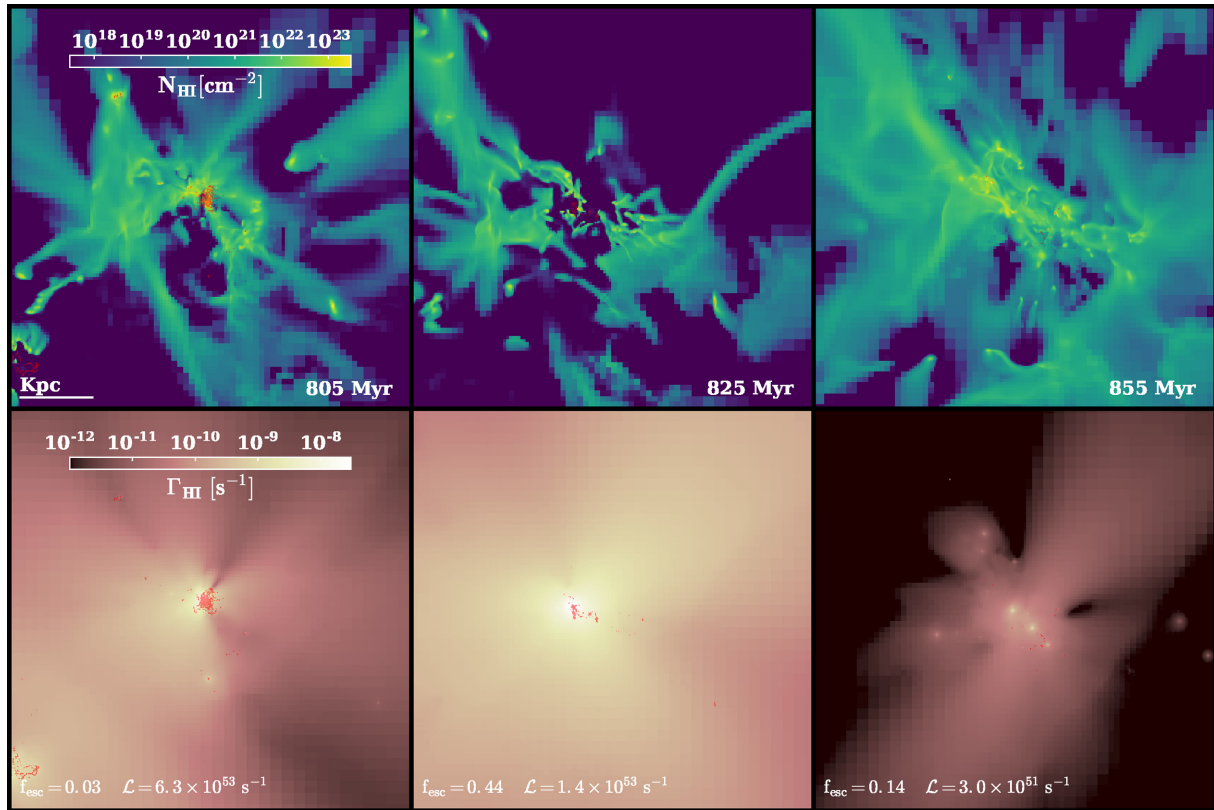


Figure 12. Time series of the main progenitor of the most massive halo in the 5 cMpc volume (binary SED) at $z \approx 6.8 - 6.4$ ($M_{\text{vir}} \approx 10^{10} M_{\odot}$, $R_{\text{vir}} \approx 9$ kpc). The upper row shows neutral hydrogen column density and the lower row shows the line-of-sight average photoionization rate. The lower limit for the column density maps, of $N_{\text{H I}} = 3 \times 10^{17} \text{ cm}^{-2}$, roughly corresponds to a unity optical depth for the ionizing radiation. In all panels, stellar populations younger than 20 Myr are superimposed as red dots. The three columns of panels correspond to the times indicated with vertical lines in Fig. 11, demonstrating the phases before, during, and after a flash of escaping ionizing radiation. The current f_{esc} and production rate of ionizing photons for the halo is written in each $\Gamma_{\text{H II}}$ panel. Initially, there is a starburst with a very high intrinsic ionizing luminosity, but the ionizing radiation is absorbed locally by the dense ISM and only a small fraction of it escapes (left). Subsequently, SN feedback disrupts the neutral ISM enough so that the radiation efficiently breaks out (centre). Finally, SF shuts down as the dense pockets of neutral ISM are destroyed. With little SN activity, the ISM resettles and absorbs the little ionizing radiation emitted from the aging stellar populations with increasing efficiency (right).

to $\approx 7-10$ per cent escape probability per photon from $\approx 2-4$ per cent without the binaries. With the binary SED model, the volumes are also fully reionized at $z > 6$, even somewhat prematurely compared to observational constraints.

This puts our results in mild tension with estimations that a global $f_{\text{esc}} \gtrsim 20$ per cent is required to match observational constraints on reionization (e.g. Kuhlen & Faucher-Giguere 2012; Ouchi et al. 2017). These estimates, however, are based on simple analytic models for the competition between photoionization and recombination that depend on the clumping factor of gas in the IGM and the intrinsic ionizing luminosity density in the early Universe, in addition to f_{esc} . Neither of these two additional parameters are currently well constrained,⁷ so our $f_{\text{esc}} \lesssim 20$ arcsec is no cause for concern.

However, our results show a degeneracy between the efficiency of feedback and the reionization history, which is a natural outcome of the regulation f_{esc} by feedback, and does appear to generate some spread in the predicted f_{esc} . In Appendix C, we show that significantly weaker SN feedback produces very similar reionization histories as our fiducial strong SN feedback, even if the rate of SF,

and hence the production of ionizing photons,⁸ is almost an order of magnitude higher.

This implies that the global escape fractions are significantly lower with weak feedback. In Fig. 15, we confirm this relationship between the strength of feedback and f_{esc} . The plot shows the global luminosity-weighted escape fractions and production rates of ionizing photons in our 5 cMpc volume, with our fiducial rate of SNe and the four times lower SN rate directly derived from a Kroupa (2001) IMF. Indeed, the typical escape fraction with fiducial feedback, while highly fluctuating (due to the disrupting nature of strong feedback and small volume), is much higher than in the weak feedback case.

In Section 3.1, we show that even with our fiducial strong SN feedback, our galaxy stellar masses (Fig. 5) and luminosity function (Fig. 7) fall towards the upper end of observational constraints and recent models. The stellar masses can be lowered, via even stronger feedback, by roughly a factor of 2 and still be in good agreement with

⁸There is not an exact linear relationship between the number of stars formed and the number of ionizing photons produced, since successive generations of stars have higher metallicities and hence lower luminosities (see Fig. 3). However, 10 times more stars certainly produce many times more ionizing photons.

⁷Also, the Thompson optical depth Kuhlen & Faucher-Giguere (2012) calibrated their results against was a bit higher (≈ 0.09) than the current estimate (≈ 0.06) by Planck.

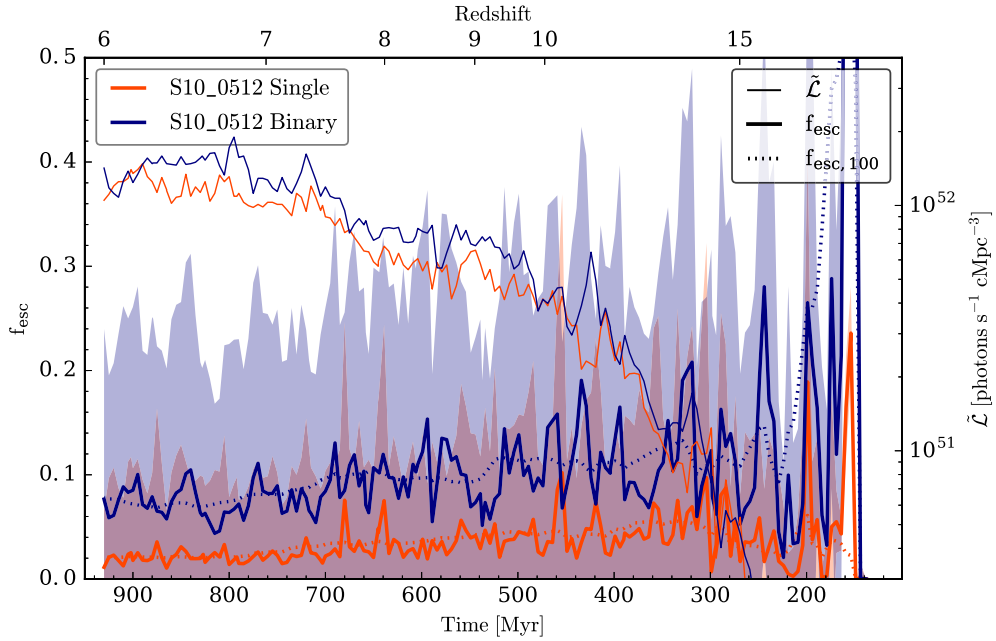


Figure 13. Time-evolution of the global luminosity-weighted escape fraction f_{esc} (thick curves; shaded regions show the luminosity-weighted variance) and production rates per volume for ionizing photons ($\tilde{\mathcal{L}}$; thin curves) for the 10 cMpc volume run with single (red) and binary (blue) SED models. Dotted lines indicate the luminosity-weighted mean f_{esc} over the last 100 Myr ($f_{\text{esc},100}$). The binary SED model results in systematically higher f_{esc} compared to the single stars SED, by a factor ≈ 3 , but also to somewhat higher production rates for ionizing photons.

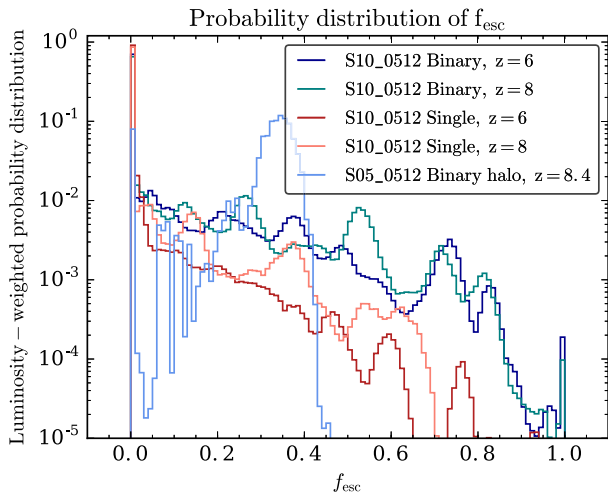


Figure 14. Luminosity-weighted probability distribution of escape fractions, f_{esc} , for selected redshifts, comparing single and binary SED models, as indicated in the legend. The distribution is defined by a ‘multimodality’, which results from a handful of galaxies existing at a given time in a bi-modal luminous and optically thin phase, with a similar fraction of the sky transparent to the ionizing radiation of each young star. We also show the probability distribution for the massive halo with the binary SED from Fig. 11 at $z = 8.4$ (≈ 600 Myr), when there is a strong peak in f_{esc} : this is to show that indeed a single halo with a high f_{esc} shows a strong bi-modal distribution in f_{esc} .

high-redshift observations and models. Based on our results with weaker feedback, such enhanced feedback simulations would likely result in similar reionization histories. Therefore, our model seems to allow for somewhat higher, but not lower, escape fractions, while still agreeing with observational constraints of the high-redshift Universe.

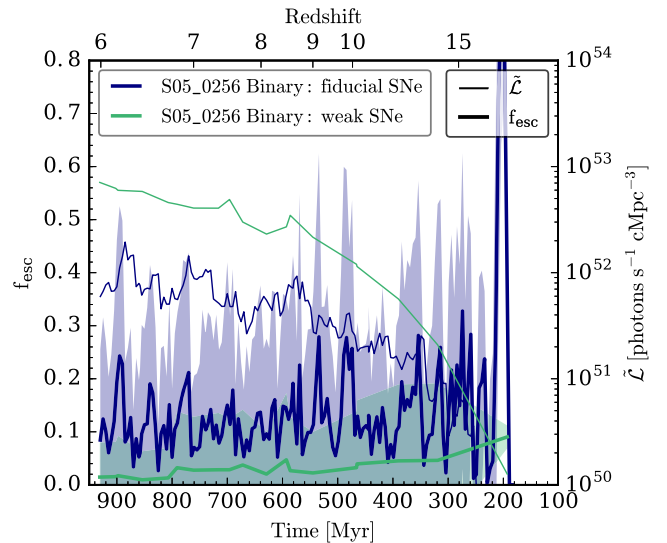


Figure 15. Time-evolution of the global luminosity-weighted escape fractions f_{esc} (variance in shaded regions) and ionizing photon production rates per volume $\tilde{\mathcal{L}}$ for the 5 cMpc volume, comparing our fiducial SN rate and a weaker SN rate as derived from a Kroupa IMF (in both cases using the binary SED model). Note that the frequency of RAMSES outputs is lower in the weak feedback case and hence fluctuations in both f_{esc} and $\tilde{\mathcal{L}}$ are likely underrepresented. The weaker SN feedback leads to about a factor of 10 higher production rates of ionizing photons than in the fiducial feedback case, but also a factor ~ 5 lower escape fractions (comparing the luminosity-weighted average for $z > 6$, which is $f_{\text{esc}} = 0.119$ for the fiducial feedback and $f_{\text{esc}} = 0.023$ with weak SNe).

Our results with binary stars, and in fact the actual event of reionization itself, appear to contradict observations of the low-redshift Universe ($z \lesssim 1.5$), where indirect measures have been made for

the escape of ionizing photons from dwarf galaxies, resulting in upper limits of a few per cent (e.g. Cowie, Barger & Trouille 2009; Bridge et al. 2010; Siana et al. 2010; Leitert et al. 2013). Reconciling this difference between low observationally estimated escape fractions at low redshift and relatively high escape fractions required to reionize the Universe is a well-known puzzle that we will not solve in this paper. There are a few possible explanations that are exciting to explore in future work. Fig. 3 demonstrates that the decline in ionizing luminosity with stellar population age steepens with increasing metallicity. Similarly, the integrated ionizing luminosities mildly decrease with increasing metallicity. Both effects suggest a possible change in SEDs between high and low redshift. If dwarf galaxies become significantly and increasingly enriched, via long-term local SF or external contamination (Anglés-Alcázar et al. 2017), their escape fractions may become very low as a result. Such a scenario, however, presents some tension with observations, as dwarf galaxies in the local Universe are not observed to become substantially enriched, with $M_* < 10^8 M_\odot$ galaxies having $< 1/10$ th solar metallicity (Kirby et al. 2013). The evolution in Fig. 14 of our 100 Myr-averaged escape fraction, $f_{\text{esc}, 100}$, does hint at the global escape fraction decreasing slowly over time, but confirming whether or not this is directly due to metallicity-dependence in the SED models is beyond the scope of this paper.

Another factor that may explain the low observed escape fractions is the stochastic nature of the escape of ionizing radiation from galaxies (Fig. 11; Kimm & Cen 2014; Ma et al. 2016; Trebitsch et al. 2017a) that makes it very difficult to derive an average escape fraction with only a few observations. Based on a post-processing of the RHD simulation of Kimm & Cen (2014) and Cen & Kimm (2015) indeed concluded that roughly ~ 100 galaxy spectra need to be stacked in order to draw meaningful conclusions on the average escape fraction.

Tempting as it is, we are reluctant to draw conclusions or preferences about different SED models from our results. Even if the two SED models we compare produce very different escape fractions and interestingly bracket current observational estimates of the reionization history, neither model produces a very good match with the observational data in Fig. 10. While this could be interpreted as some sort of uncertainty in SED models, it may just as well be a limitation of unresolved escape fractions. Presumably – and this will be attempted in future work – we could calibrate our unresolved escape fraction, with $f'_{\text{esc}} \gtrsim 1$ for the single-stars SED model and $f'_{\text{esc}} \lesssim 1$ for the binary stars, and produce good matches with observations using either SED model. We cannot yet say for sure if the escape of radiation from the ISM is resolved in our simulations, nor can we tell whether it is overestimated or underestimated, and hence it is not timely to rule out any SED models. We suffice to conclude that in the framework of our models, the inclusion of binary stars has a huge impact on the reionization history and makes it easy to reionize the Universe by $z \approx 6$.

We do not include active galactic nuclei (AGN) in our simulations, nor do we consider the effects of molecular cooling or PopIII stars. AGN are expected to become relevant in galaxies that are more massive than those currently captured in our simulations (Trebitsch et al. 2017b; Mitchell et al. 2018). We aim in the next generation of larger volume SPHINX simulations to study the possible contribution of more massive galaxies and AGN to reionization. However, their contribution to the EoR ionizing background is at best uncertain (see the debate in Chardin, Puchwein & Haehnelt 2016; D’Aloisio et al. 2016; Parsa, Dunlop & McLure 2017). Regardless, the inclusion of binary stars in the emission from high-redshift stellar populations removes the *need* for any other sources of reionization than stars.

The possible contribution from metal-free (PopIII) stars has been considered in recent state-of-the-art models (Wise et al. 2014; Kimm et al. 2017) and the general conclusion is that they have relatively little direct impact on reionization at $z < 10$. The impact of PopIII stars during the EoR is an interesting question, but due to the large uncertainty in the PopIII IMF, a current inclusion of PopIII physics really constitutes an additional set of free parameters, which we prefer to skip in the first generation of our simulation suite.

For similar reasons of simplicity and transparency, we have chosen to not model the formation and destruction of molecular hydrogen. The first generation of stars was made possible by primordial molecular hydrogen formation and cooling, while successive generations formed via more efficient gas cooling catalysed by metals. In the current SPHINX simulations, instead of modelling the complex molecular hydrogen formation channels, we have imitated the effects of primordial molecular hydrogen by calibrating the initial gas metallicity in our simulations to reach a similar *initial* epoch and efficiency of SF as in zoom-simulations where primordial molecular hydrogen formation was included (using the models described in Kimm et al. 2017).

5 CONCLUSIONS

This paper describes the SPHINX suite of cosmological simulations, the first non-zoom radiation-hydrodynamical simulations of reionization that capture the large-scale reionization process and simultaneously start to predict the escape fraction, f_{esc} , of ionizing radiation from thousands of galaxies. Our series of 5 and 10 cMpc wide volumes resolve haloes down to the atomic cooling limit and model the ISM of galaxies with ~ 10 pc resolution. We select our cosmological ICs out of 60 candidates to minimize the impact of cosmic variance on the volume-emissivity of ionizing photons and to maintain consistent reionization histories across different volumes.

Owing to strong SN feedback, our haloes are in good agreement with high-redshift observations, as well as recent state-of-the-art models, of the SMHM, SFR versus halo mass, and, most importantly, the 1500 Å UV luminosity function at $z = 6$ (Fig. 7).

We study the effect of binary stars on reionization. Due to mass transfer and mergers between binary companion stars, SED models that include binary stars predict higher integrated ionizing luminosities for stellar populations as well as a much shallower decline of luminosity with stellar age (Stanway et al. 2016). We run and compare two sets of SPHINX simulations: one with the BPASS SED model (Eldridge et al. 2007) that includes binary stars, and one with the Bruzual & Charlot (2003) model, which does not. Using the M1 moment method for RT, we inject into our volumes the exact ionizing luminosities dictated by those SED models, given the metallicity, age, and mass of each stellar population particle, and without any calibration in unresolved escape fractions.

The reionization histories strongly differ in the models with and without binary stars (Fig. 9). The different reionization histories bracket the observed constraints, with the binaries model reionizing at $z \approx 7$, slightly earlier than observations predict, while the model with single stars does not ionize the volume by $z = 6$.

Because the escape fraction is regulated by feedback, as was demonstrated by Kimm et al. (2017) and later by Trebitsch et al. (2017a), it fluctuates strongly with time in an individual galaxy (Fig. 11), with brief flashes of radiation during which the galaxy satisfies the two conditions of being luminous and having an ISM disrupted enough for ionizing radiation to escape. The binary SED model consistently results in (luminosity-weighted) mean $f_{\text{esc}} \approx 7$ –

10 per cent, with a large scatter. This is a factor ≈ 3 higher than that for the singles-only SED model (Fig. 13).

The higher escape fractions are due to the combination of feedback and the shallower decline in stellar luminosities with binaries: by disrupting the ISM and clearing away dense gas, feedback simultaneously suppresses SF and increases the local f_{esc} . With binary stars, more photons can escape, and for a longer time, after this ISM disruption, leading to larger globally averaged escape fractions. The higher escape fractions are the primary reason for the much earlier reionization with binaries, but the higher integrated luminosity with binaries also plays a subdominant role.

Our reionization histories are robust to changes in resolution, volume size, and, surprisingly, to changes in the SN feedback efficiency. The robustness to SN feedback is an outcome of an apparent balance between ionizing luminosities and escape fractions, which scale down and up, respectively, with increased feedback efficiency (Fig. 15).

We will follow up this work with an analysis of how escape fractions vary with halo mass and how haloes of different masses contribute to reionization. We will also use the SPHINX simulations to study the back-reaction of suppressed galaxy growth via reionization and to predict the observational properties of extreme-redshift galaxies, which will become increasingly visible to us when the *JWST* comes online.

ACKNOWLEDGEMENTS

We are grateful to the reviewer, John Wise, for comments that strengthened the paper. We thank Dominique Aubert, Leindert Boogaard, Julien Devriendt, Yohan Dubois, Peter Mitchell, Ali Rahmati, Benoit Semelin, and Maxime Trebitsch for useful discussions, and Andreas Bleuler for very useful contributions to the optimization of RAMSES-RT. JR and JB acknowledge support from the ORAGE project from the Agence Nationale de la Recherche under grant ANR-14-CE33-0016-03. HK thanks the Beecroft fellowship, the Nicholas Kurti Junior Fellowship, and Brasenose College. TK is supported by the National Research Foundation of Korea to the Center for Galaxy Evolution Research (no. 2017R1A5A1070354) and in part by the Yonsei University Future-leading Research Initiative of 2017 (RMS2-2017-22-0150). TG is grateful to the LABEX Lyon Institute of Origins (ANR-10-LABX-0066) of the Université de Lyon for its financial support within the programme ‘Investissements d’Avenir’ (ANR-11-IDEX-0007) of the French government operated by the National Research Agency (ANR). Support by ERC Advanced Grant 320596 ‘The Emergence of Structure during the Epoch of reionization’ is gratefully acknowledged. The results of this research have been achieved using the PRACE Research Infrastructure resource SuperMUC based in Garching, Germany. We are grateful for the excellent technical support provided by the SuperMUC staff. Preparations and tests were also performed at the Common Computing Facility (CCF) of the LABEX Lyon Institute of Origins (ANR-10-LABX-0066), and on the GENCI national computing centres at CCRT and CINES (DARI grant number x2016047376). Available at <https://sphinx.univ-lyon1.fr/>.

REFERENCES

- Anglés-Alcázar D., Faucher-Giguère C.-A., Kereš D., Hopkins P. F., Quataert E., Murray N., 2017, *MNRAS*, 470, 4698
- Aubert D., Pichon C., Colombi S., 2004, *MNRAS*, 352, L376
- Bañados E. et al., 2018, *Nature*, 553, 473
- Behroozi P. S., Wechsler R. H., Conroy C., 2013, *ApJ*, 770, 57
- Blondin J. M., Wright E. B., Borkowski K. J., Reynolds S. P., 1998, *ApJ*, 500, 342
- Bonazzola S., Falgarone E., Heyvaerts J., Perault M., Puget J. L., 1987, *A&A*, 172, 293
- Booth C. M., Agertz O., Kravtsov A. V., Gnedin N. Y., 2013, *ApJ*, 777, L16
- Bouwens R. J. et al., 2015, *ApJ*, 803, 34
- Bouwens R. J., Oesch P. A., Illingworth G. D., Ellis R. S., Stefanon M., 2017, *ApJ*, 843, 129
- Bridge C. R. et al., 2010, *ApJ*, 720, 465
- Bruzual G., Charlot S., 2003, *MNRAS*, 344, L1000
- Calverley A. P., Becker G. D., Haehnelt M. G., Bolton J. S., 2010, *MNRAS*, 412, 2543
- Cen R., Kimm T., 2015, *ApJ*, 801, L25
- Chardin J., Puchwein E., Haehnelt M. G., 2016, *MNRAS*, 465, 3429
- Chen P., Norman M. L., Xu H., Wise J. H., 2017, *Astrophys. J.*, preprint (arXiv:1705.00026)
- Commerçon B., Debout V., Teyssier R., 2014, *A&A*, 563, 11
- Cowie L. L., Barger A. J., Trouille L., 2009, *ApJ*, 692, 1476
- D’Aloisio A., Sanderbeck P. R. U., McQuinn M., Trac H., Shapiro P. R., 2016, *MNRAS*, 468, 4691
- D’Aloisio A., McQuinn M., Davies F. B., Furlanetto S. R., 2018, *MNRAS*, 473, 560
- Dijkstra M., Loeb A., 2009, *MNRAS*, 396, L377
- Eldridge J. J., Izzard R. G., Tout C. A., 2007, *MNRAS*, 384, 1109
- Fan X., Carilli C. L., Keating B., 2006, *ARA&A*, 44, 415
- Federrath C., Klessen R. S., 2012, *ApJ*, 761, 156
- Ferland G. J., Korista K. T., Verner D. A., Ferguson J. W., Kingdon J. B., Verner E. M., 1998, *PASP*, 110, 761
- Finlator K., Dave R., Ozel F., 2011, *ApJ*, 743, 169
- Gatto A. et al., 2016, *MNRAS*, 466, 1903
- Geen S., Rosdahl J., Blaizot J., Devriendt J., Slyz A., 2015, *MNRAS*, 448, 3248
- Girichidis P. et al., 2016, *ApJ*, 816, L19
- Gnedin N. Y., 2014, *ApJ*, 793, 29
- Gnedin N. Y., 2016, *ApJ*, 833, 66
- Gnedin N. Y., Fan X., 2006, *ApJ*, 648, 1
- Gnedin N. Y., Kaurov A. A., 2014, *ApJ*, 793, 30
- Guillet T., Teyssier R., 2011, *J. Comput. Phys.*, 230, 4756
- Haardt F., Madau P., 1996, *ApJ*, 461, 20
- Hahn O., Abel T., 2011, *MNRAS*, 415, 2101
- Hanasz M., Lesch H., Naab T., Gawryszczak A., Kowalik K., Wóltański D., 2013, *ApJ*, 777, L38
- Harikane Y. et al., 2018, *PASJ*, 70, S11
- Hopkins P. F., Quataert E., Murray N., 2012, *MNRAS*, 421, 3522
- Hopkins P. F., Kereš D., Oñorbe J., Faucher-Giguère C.-A., Quataert E., Murray N., Bullock J. S., 2014, *MNRAS*, 445, 581
- Iliev I. T., Mellema G., Ahn K., Shapiro P. R., Mao Y., Pen U.-L., 2013, *MNRAS*, 439, 725
- Inoue A. K. et al., 2018, *PASJ*, 70, 55
- Katz N., Weinberg D. H., Hernquist L., 1996, *ApJS*, 105, 19
- Katz H., Kimm T., Sijacki D., Haehnelt M. G., 2017, *MNRAS*, 468, 4831
- Katz H., Kimm T., Haehnelt M., Sijacki D., Rosdahl J., Blaizot J., 2018, *MNRAS*, 478, 4986
- Kim C.-G., Ostriker E. C., 2015, *ApJ*, 802, 99
- Kimm T., Cen R., 2014, *ApJ*, 788, 121
- Kimm T., Cen R., Devriendt J., Dubois Y., Slyz A., 2015, *MNRAS*, 451, 2900
- Kimm T., Cen R., Rosdahl J., Yi S. K., 2016, *ApJ*, 823, 52
- Kimm T., Katz H., Haehnelt M., Rosdahl J., Devriendt J., Slyz A., 2017, *MNRAS*, 465, 4826
- Kimm T., Haehnelt M., Blaizot J., Katz H., Michel-Dansac L., Garel T., Rosdahl J., Teyssier R., 2018, *MNRAS*, 475, 4617
- Kirby E. N., Cohen J. G., Guhathakurta P., Cheng L., Bullock J. S., Gallazzi A., 2013, *ApJ*, 779, 102
- Kroupa P., 2001, *MNRAS*, 322, L231

Kuhlen M., Faucher-Giguere C.-A., 2012, *MNRAS*, 423, 862
 Leitet E., Bergvall N., Hayes M., Linné S., Zackrisson E., 2013, *A&A*, 553, A106
 Levermore C. D., 1984, *J. Quant. Spectrosc. Radiat. Transfer*, 31, 149
 Livermore R. C., Finkelstein S. L., Lotz J. M., 2017, *ApJ*, 835, 113
 Ma X., Hopkins P. F., Kasen D., Quataert E., Faucher-Giguere C.-A., Keres D., Murray N., Strom A., 2016, *MNRAS*, 459, 3614
 Ma X. et al., 2018, *MNRAS*, 478, 1694
 Martizzi D., Faucher-Giguere C.-A., Quataert E., 2015, *MNRAS*, 450, 504
 Mitchell P. D., Blaizot J., Devriendt J., Kimm T., Michel-Dansac L., Rosdahl J., Slyz A., 2018, *MNRAS*, 474, 4279
 Ocvirk P. et al., 2015, *MNRAS*, 463, 1462
 Ocvirk P., Aubert D., Deparis N., Lewis J., 2018, preprint (arXiv:1803.02434)
 Oke J. B., Gunn J. E., 1983, *ApJ*, 266, 713
 Ouchi M. et al., 2017, *PASJ*, 70, S13
 Pakmor R., Pfrommer C., Simpson C. M., Springel V., 2016, *ApJ*, 824, L30
 Parsa S., Dunlop J. S., McLure R. J., 2017, *MNRAS*, 474, 2904
 Pawlik A. H., Rahmati A., Schaye J., Jeon M., Vecchia C. D., 2016, *MNRAS*, 466, 960
 Planck Collaboration I, 2014, *A&A*, 571, A1
 Raseria Y., Teyssier R., 2006, *A&A*, 445, 1
 Read J. I., Iorio G., Agertz O., Fraternali F., 2017, *MNRAS*, 467, 2019
 Rosdahl J., Teyssier R., 2015, *MNRAS*, 449, 4380
 Rosdahl J., Blaizot J., Aubert D., Stranex T., Teyssier R., 2013, *MNRAS*, 436, 2188
 Rosdahl J., Schaye J., Teyssier R., Agertz O., 2015, *MNRAS*, 451, 4553
 Rosdahl J., Schaye J., Dubois Y., Kimm T., Teyssier R., 2017, *MNRAS*, 466, 11
 Rosen A., Bregman J. N., 1995, *ApJ*, 440, 634
 Safarzadeh M., Scannapieco E., 2016, *ApJ*, 832, L9
 Schroeder J., Mesinger A., Haiman Z., 2012, *MNRAS*, 428, 3058
 Shull J. M., van Steenberg M. E., 1985, *ApJ*, 298, 268
 Siana B. et al., 2010, *ApJ*, 723, 241
 Smith A., Bromm V., Loeb A., 2016, *MNRAS*, 464, 2963
 So G. C., Norman M. L., Reynolds D. R., Harkness R. P., 2014, *ApJ*, 789, 149
 Sobacchi E., Mesinger A., 2015, *MNRAS*, 453, 1843
 Stanway E. R., Eldridge J. J., Becker G. D., 2016, *MNRAS*, 456, 485
 Strömgren B., 1939, *ApJ*, 489, 526
 Teyssier R., 2002, *A&A*, 385, 337
 Thompson T. A., Quataert E., Murray N., 2005, *ApJ*, 630, 167
 Thornton K., Gaudlitz M., Janka H.-T., Steinmetz M., 1998, *ApJ*, 500, 95
 Toro E. F., Spruce M., Speares W., 1994, *Shock Waves*, 4, 25
 Trebitsch M., Blaizot J., Rosdahl J., Devriendt J., Slyz A., 2017a, *MNRAS*, 470, 224
 Trebitsch M., Volonteri M., Dubois Y., Madau P., 2017b, *MNRAS*, preprint (arXiv:1712.05804)
 Tweed D., Devriendt J., Blaizot J., Colombi S., Slyz A., 2009, *A&A*, 506, 647
 Verner D. A., Ferland G. J., Korista K. T., Yakovlev D. G., 1996, *ApJ*, 465, 487
 Westera P., Lejeune T., Buser R., Cuisinier F., Bruzual G., 2002, *A&A*, 381, 524
 Wise J. H., Cen R., 2009, *ApJ*, 693, L984
 Wise J. H., Demchenko V. G., Halicak M. T., Norman M. L., Turk M. J., Abel T., Smith B. D., 2014, *MNRAS*, 442, 2560
 Wyithe S., Bolton J. S., 2010, *MNRAS*, 412, 1926
 Xu H., Wise J. H., Norman M. L., Ahn K., O’Shea B. W., 2016, *ApJ*, 833, 84

APPENDIX A: LUMINOSITY FUNCTIONS

For future comparisons to models and/or observations, we show in Table A1 our predicted 1500 Å luminosity functions for our 5 and 10 cMpc wide volumes, with the binary SED, at $z = 6, 8, \text{ and } 10$. These luminosity functions are also plotted in Fig. A1.

Table A1. SPHINX predictions for the 1500 Å luminosity function with binary stars at $z = 6, 8, \text{ and } 10$. The luminosity functions, ϕ_5 and ϕ_{10} , are from the 5 and 10 cMpc wide volumes, respectively, and are given in units of [$\text{Mag}^{-1} \text{cMpc}^{-3}$].

M_{AB}	$z = 10$		$z = 8$		$z = 6$	
	ϕ_5	ϕ_{10}	ϕ_5	ϕ_{10}	ϕ_5	ϕ_{10}
−20.5	0	0	0	0.001	0	0.001
−19.5	0	0	0	0.001	0	0.001
−18.5	0	0.001	0	0.004	0.008	0.01
−17.5	0	0.004	0	0.012	0.008	0.017
−16.5	0.008	0.012	0.032	0.023	0.032	0.05
−15.5	0.016	0.034	0.56	0.068	0.096	0.106
−14.5	0.048	0.083	0.104	0.124	0.168	0.159
−13.5	0.160	0.140	0.264	0.235	0.256	0.306
−12.5	0.256	0.242	0.472	0.374	0.496	0.486
−11.5	0.488	0.344	1.096	0.514	1.072	0.674
−10.5	0.816	0.421	1.496	0.678	1.784	0.909
−9.5	0.744	0.385	1.640	0.728	2.728	1.147
−8.5	0.776	0.441	1.880	0.954	3.176	1.52
−7.5	0.800	0.394	1.944	0.993	3.712	1.907
−6.5	0.224	0.168	1.136	0.616	3.448	1.685

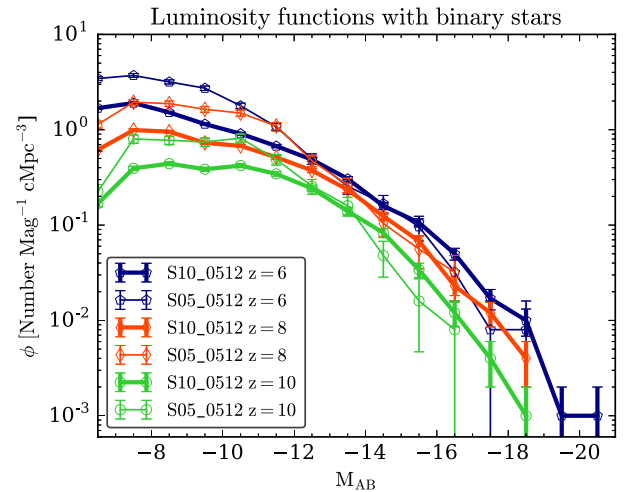


Figure A1. Predicted 1500 Å luminosity functions with binary stars at $z = 6, 8, \text{ and } 10$, with Poissonian error bars.

APPENDIX B: RESOLUTION CONVERGENCE

In this appendix, we compare the main results of our fiducial simulations to those acquired with lower resolution, in order to show that they are not significantly affected by minor variations in spatial and mass resolution.

Fig. B1 shows the $z = 6$ SMHM relation for resolution variations in our 5 cMpc volume (with the binary SED model). The thickest (blue) curve shows our high-resolution case, where the DM mass resolution is $3.1 \times 10^4 M_{\odot}$ and the maximum physical resolution at $z = 6$ is 10.9 pc. The medium-thickness (red) curve represents a run with our fiducial mass resolution, where the DM mass resolution is degraded to $2.5 \times 10^5 M_{\odot}$ per DM particle, but the stellar mass and physical resolution remain fixed. The thinnest (green) curve represents another run where we have also degraded the maximum physical resolution, which is now at 21.8 pc at $z = 6$. These resolution changes have little and non-systematic effects on the SMHM relation. The most noticeable difference is a hint of systematically higher stellar mass for the most massive haloes with

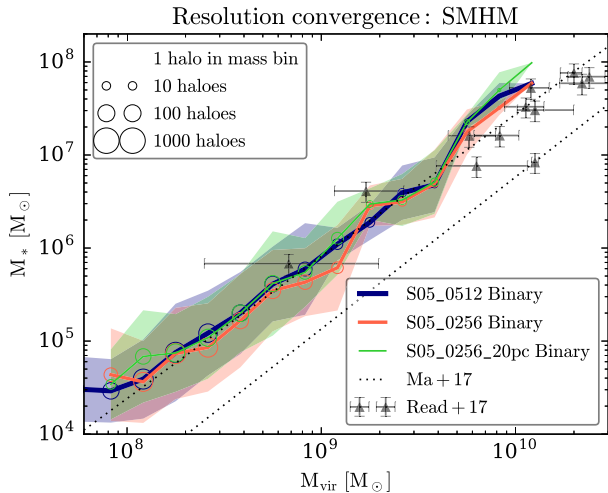


Figure B1. Resolution variations of the SMHM relation in our 5 cMpc volume simulations. The thickest (blue) curve represents the high-resolution run, intermediate thickness (red) represents a run with degraded DM mass resolution by a factor of 8, and the thinnest (green) curve represents a run with the same degradation in mass and an additional degradation of the maximum physical resolution (≈ 20 pc instead of 10). Observations and recent predictions from simulations are included as in the main text. Circles show the number of haloes in each mass bin. The changes in resolution have little effect on the SMHM relation.

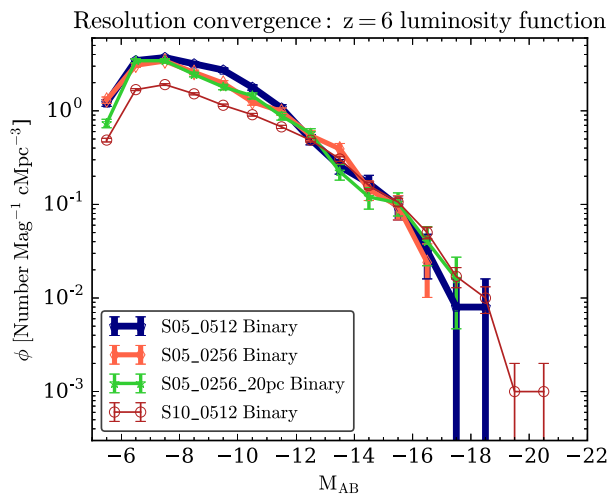


Figure B2. Resolution variations of the $z = 6$ luminosity function (with Poissonian error bars). We show the high-resolution run for the 5 cMpc volume in blue and compare to the same volume with degraded mass resolution (orange) and also degraded physical resolution (green). Changing the DM mass resolution and the maximum physical resolution has little systematic effect, except there is a hint of more galaxies at the faint end with higher DM mass resolution. Changing the ICs has a much larger effect: in red we show the results for our 10 cMpc volume, with the fiducial resolution matching s05_256.

degraded physical resolution, but this may as well be due to low number statistics.

We show how the luminosity function for the 5 cMpc volume changes with resolution in Fig. B2. There is little systematic difference for the different resolution runs, except for a hint of slightly more galaxies at the faint end with higher DM mass resolution. Comparing with the larger volume (shown in red), the luminosity function is clearly much more sensitive to the cosmological ICs

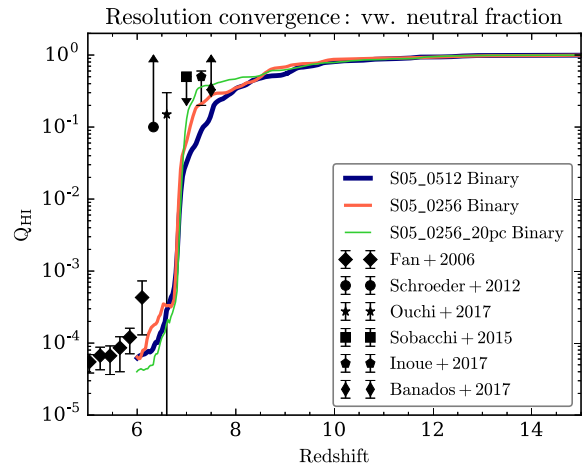


Figure B3. Resolution variations of the redshift evolution of the volume-filling neutral fraction, Q_{HII} , with the same resolution variations (in the 5 cMpc volume) as in Figs B1 and B2. Lowering the resolution has little effect on the reionization history.

than to factor-few changes in resolution. From Fig. 7, it is also clear that using different SED models has a larger effect than those resolution changes. There are, however, likely stellar mass resolution effects at the low-luminosity end, manifested in the down-turn in the luminosity functions in the faintest bin. Our galaxies with $M_{\text{AB}} > -9.5$ contain fewer than 100 stellar particles on average; their SF histories are overly discrete and likely underestimated.

In Fig. B3, we show how the same variations in resolution affect the reionization history. The aforementioned variations in resolution have minor effects on the reionization history that do not appear to be systematic. These minor variations in the Q_{HII} evolution are likely the result of the stochasticity of starbursts and feedback in our relatively small simulation volume in the calibration simulations. We can confirm that simply varying the random seeds for SF has similar-amplitude effects on the reionization history as these resolution variations.

Note that we have not studied a degraded stellar mass resolution. We expect that variations in the stellar mass resolution within sensible limits has little effect, since we inject individual SN explosions rather than instantaneously injecting the total SN energy for the mass of each stellar population particle (the latter would translate into stronger resolution effects, with fewer, more energetic SN explosions). Furthermore, decreasing the stellar particle mass significantly from our $1000 M_{\odot}$ brings us into a questionable regime where the IMF is no longer sampled by a single particle and we need to consider more sophisticated models for stellar populations.

APPENDIX C: CALIBRATION OF SN FEEDBACK

We now demonstrate how our SN feedback model is calibrated to match constraints to the 1500 \AA UV luminosity function and the SMHM relation.

In Fig. C1, we compare simulated 1500 \AA luminosity functions at $z = 6$ in our 5 cMpc volume (with fiducial resolution) with observations from Bouwens et al. (2017) and Livermore et al. (2017). The thin green curve shows the luminosity function for an uncalibrated SN rate derived from a Kroupa (2001) IMF, with 10 Type II SN explosions per $10^3 M_{\odot}$. The thick blue curve shows the results for our fiducial SN feedback, where the rate of SN explosions has been

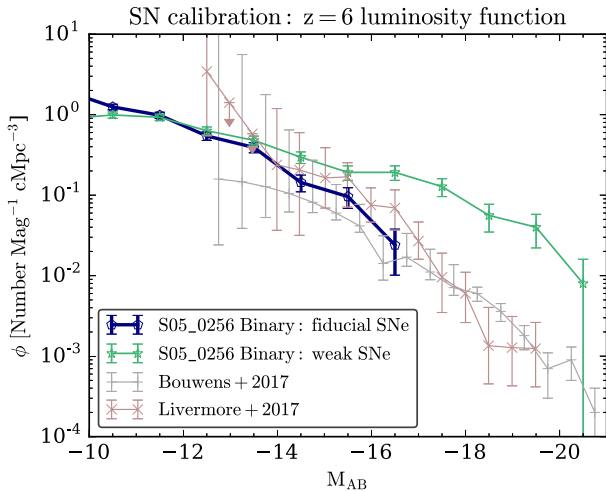


Figure C1. SN rate calibration effects on the predicted luminosity function at 1500 \AA , with two sets of $z = 6$ observations included for comparison. The error bars for the SPHINX data are Poissonian. The ‘weak’ SN rate derived from a Kroupa (2001) IMF results in an unrealistic luminosity function, while our calibrated, four-times boosted SN rate produces good agreement with observations (within the luminosity range captured by this 5 cMpc wide volume).

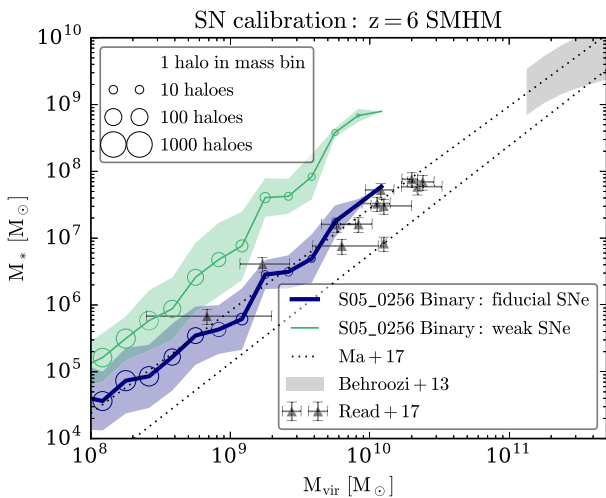


Figure C2. SMHM relation for our fiducial and weak, uncalibrated, SN feedback, as indicated in the legend. The sizes of the circles indicate the number of haloes in each mass bin and the shaded regions indicate the standard deviation. Calibrated SN feedback results in a good agreement with (local Universe) observations.

boosted four-fold, so that 40 SN explosions occur per $10^3 M_\odot$. Both are run with the binary SED model (which is also used to calculate the luminosity of each galaxy; as usual dust attenuation is ignored). The lower SN rate is clearly insufficient to produce a realistic luminosity function, while the fiducial boosted feedback produces a luminosity function in reasonable agreement with the observational constraints. As we have seen in Fig. 7, this agreement for the fiducial calibrated SN feedback holds both in the case of higher mass resolution and for an eight times larger volume.

Fig. C2 shows a comparison, for the same two simulations, of the predicted SMHM relation. We include the local Universe observations from Read et al. (2017) and the $z = 6$ relation derived by Behroozi et al. (2013). Our fiducial SN feedback results in an

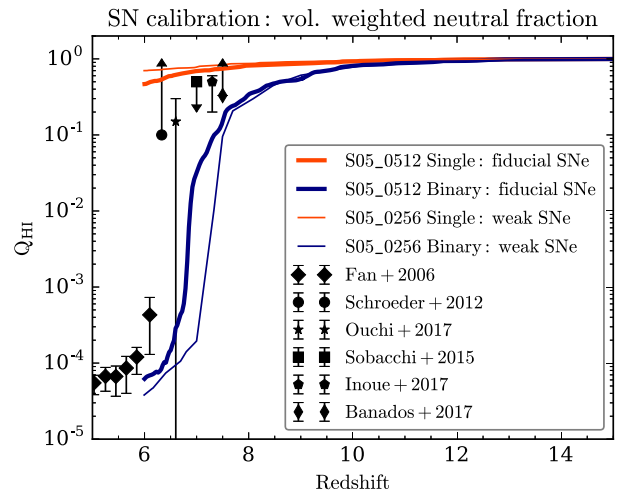


Figure C3. Calibration effects on the redshift evolution of the volume-filling neutral fraction, Q_{HII} . We show the 5 cMpc volume run with both single and binary SED models, as indicated in the legend, as well as with our fiducial and weak SN feedback, and compare to the same observational estimates as in Fig. 9. Reducing the rate of SNe by a factor of 4 has little effect, neither on the reionization history nor the very significant speed-up resulting from the inclusion of binary stars.

SMHM relation that agrees well with local Universe observations and does not appear in conflict with high-redshift constraints. The uncalibrated feedback produces much higher stellar masses, by almost an order of magnitude at the high-mass end.

Our fiducial four-fold boost in the rate of SN explosions is a simple substitute for an unknown combination of the following and possibly incomplete list of factors: (i) uncertainty in the IMF and hence the rate of SN explosions, (ii) resolution, which may play a role, but likely not a large one, as our resolution has been demonstrated to produce results that are resolution-converged and not subject to severe overcooling, (iii) uncertainty in gas cooling rates, which affects the final momentum gained in the remnants of SN explosions, and (iv) lack of complementary feedback physics, such as cosmic rays, stellar winds, or AGN, though the latter is unlikely in the mass range for galaxies captured in our simulations (Trebitsch et al. 2017b).

Regardless, our main result – of a large difference in the reionization histories produced by single and binary stellar populations – is robust with respect to the feedback calibration. Fig. C3 shows that the reionization histories are very similar if the feedback is not boosted, and the same difference remains between single and binary stellar populations. It may seem counter-intuitive that reionization progresses as efficiently with weak SN feedback, but this is due to the feedback regulation of both SF and f_{esc} . Many more stars are produced with the weaker feedback model and this leads to larger ionizing luminosities. However, the SNe also become less efficient at disrupting the ISM, leading to a smaller fraction of photons that escape into the IGM. With the higher luminosities but lower escape fractions, a comparable number of ionizing photons escapes the galaxies compared to our fiducial model.

APPENDIX D: SED PROPERTIES

The ionizing luminosities of stellar particles in our simulations, as well as the properties of the three radiation groups, are based on two SED models, which each provide a set of spectra binned by metallic-

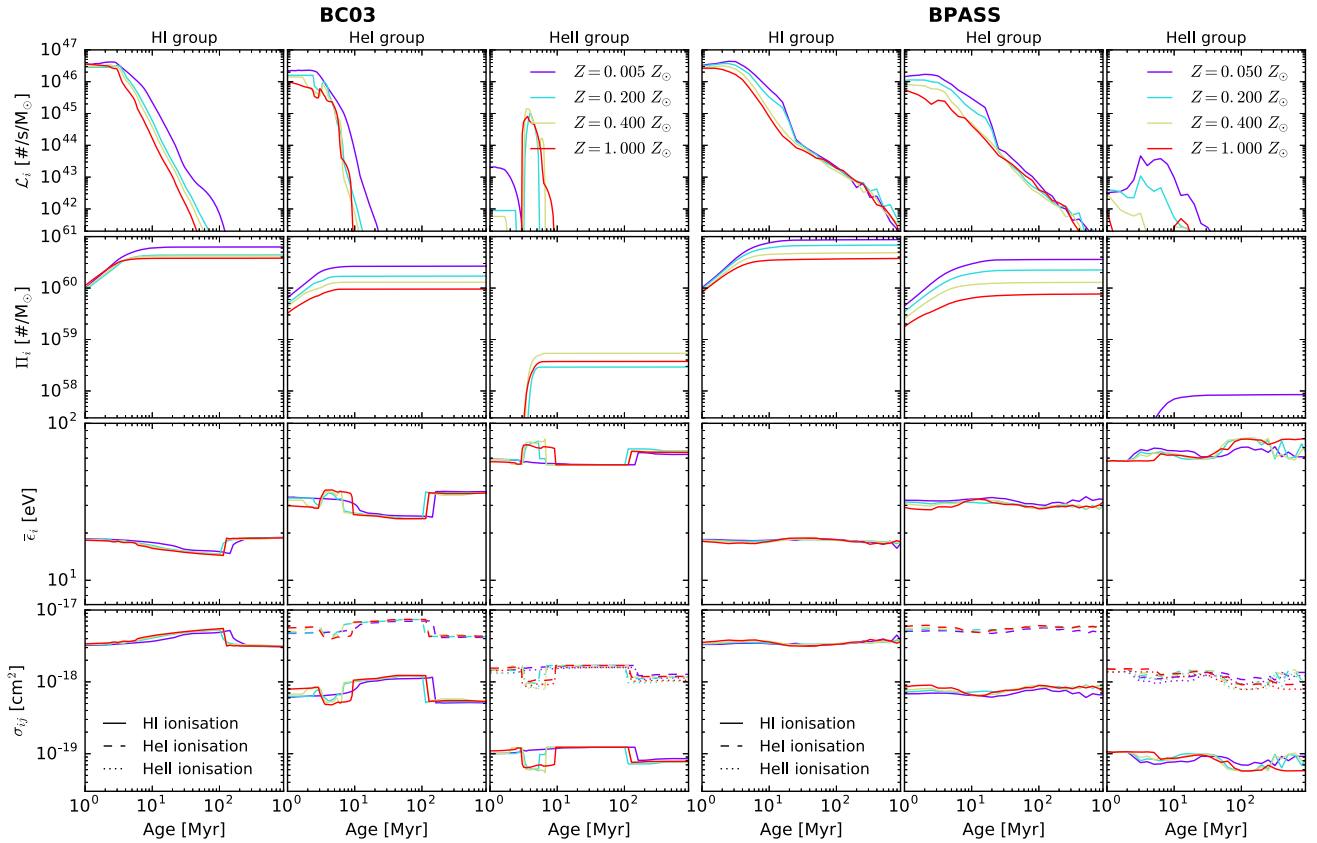


Figure D1. Properties of the two SED models used in this work. BC03, on the left, is the single star model from Bruzual & Charlot (2003), while BPASS, on the right, is the model from Eldridge et al. (2007), which includes binary stars. For each SED model, the three columns are for the three radiation groups (H I, He I, and He II-ionizing), defined in Table 3. The rows, from top to bottom, show the stellar age evolution of the ionizing luminosity \mathcal{L}_i (number of ionizing photons in radiation group i per solar mass per time), the integrated luminosity Π_i (total number of ionizing photons emitted in group i per solar mass), the average energy per photon, $\bar{\epsilon}_i$, over the energy range defined by group i , and photon number-weighted average cross sections, σ_{ij} , over the energy range defined by group i for photoionizing species j (in H I, He I, and He II), using the frequency-dependences for photoionization from Verner et al. (1996). In each plot, the colours denote the metallicity assumed for the stellar population, as indicated in the legend in the top-right panel for each SED model.

ity and population age (assuming an instantaneous formation time), and normalized to M_\odot .

One set of simulations uses (Bruzual & Charlot 2003, bc03), which includes only single star systems. Here, we use the model generated with the semi-empirical BaSeL 3.1 stellar atmosphere library (Westera et al. 2002) and a Kroupa (2001) IMF. The other set of simulations uses the BPASS model (Eldridge et al. 2007), which includes binary stars, and has an IMF closest to Kroupa (2001), with slopes of -1.3 from 0.1 to $0.5 M_\odot$ and -2.35 from 0.5 to $100 M_\odot$. Fig. D1 shows in detail the age- and metallicity-dependence of the stellar population luminosities, number weighted mean photon energies, and cross sections, for all three radiation groups (defined in Table 3), integrated from the two SED spectra for bins of population age and metallicity.

From each SED spectrum (in units of $\text{erg s}^{-1} M_\odot^{-1} \text{\AA}^{-1}$), we extract and tabulate age- and metallicity-dependent ionizing luminosities, average energies, number-, and energy-weighted cross sections for all radiation groups, by integrating over the wavelength interval defined for each group.⁹ Using linear interpolation, we then re-bin the tables in age and metallicity (eight bins) so that the increment

is linear in log-space, i.e. $\Delta \log(\text{age}/\text{Gyr}) = 0.02$ is the same for every age-interval (giving 266 bins for BC03, 209 bins for BPASS) and $\Delta \log(Z/Z_\odot) (=0.43$ for BC03, 0.23 for BPASS) is the same for every metallicity-interval. The purpose of the re-binning is to speed up the age- and metallicity-interpolation performed for every star particle in every RHD time-step. The lowest tabulated zero-age is a special case for the interpolation, since we cannot tabulate the logarithm of zero.

For each re-binned age bin, we integrate and tabulate the cumulative luminosity (number of photons per solar mass emitted up to given age), assuming constant metallicity. We then use this re-binned table to extract the number of photons emitted by a stellar particle by comparing the cumulative luminosity before and after the RHD timestep. We use the cumulative luminosity rather than simply multiplying the instantaneous luminosity by the timestep length, because if the timestep happens to be very large, short bursts in luminosity may be lost entirely. Using the cumulative luminosity ensures that these unresolved bursts are still accounted for in the photon budget.

For metallicities outside the table limits, we use the lowest or highest tabulated metallicity (this is irrelevant for age, which is always within the tabulated limits). We feel this is a more conservative option than to apply extrapolation outside the metallicity limits: the BC03 model reaches 10 times lower metallicity than BPASS, and

⁹For BC03, the ages range from zero to 13.8 Gyr, and for BPASS from zero to 20 Gyr. The metallicities range from 0.005 – $5 Z_\odot$ for BC03 and 0.05 – $2 Z_\odot$ for BPASS.

lower metallicity generally leads to higher ionizing luminosity (see Fig. D1). Hence, if there is an underestimate of luminosities at very low metallicities due to our lack of extrapolation, the underestimate should be more exaggerated with BPASS than with BC03, i.e. we are then underestimating the difference between BPASS and BC03.

Every 10 coarse time-steps, we update the photoionization cross sections and energies for the radiation groups in our simulations to represent the luminosity-weighted average of all emitting sources in our simulations. The details of this process are described in appendix B2 in Rosdahl et al. (2013). Note that since stellar population particles have different ages and metallicities, and hence different spectra as defined by the assumed SED model, the emission of photons into a radiation group cannot be exactly energy-conserving and photon-number conserving at the same time. Given the energy per

photon defined for the group, we can choose to emit either (i) the exact amount of energy per time, leaving a small error in the number of photons per time, due to the difference in the particle spectrum over the group frequency interval from the ‘average’ group spectrum, or (ii) the exact number of photons, sacrificing in the same way the exact energy luminosity. In this work, we have chosen the latter, as the number of ionizing photons is more important in the context of reionization.

This paper has been typeset from a $\text{\TeX}/\text{\LaTeX}$ file prepared by the author.